

High repetition rate ultrafast electron diffraction with direct electron detection

F. Rodriguez Diaz¹, M. Mero¹, K. Amini^{1,*}

¹Max-Born-Institut, Max-Born-Straße 2A, 12489 Berlin, Germany

*corresponding author e-mail: amini@mbi-berlin.de

ABSTRACT

Ultrafast electron diffraction (UED) instruments typically operate at kHz or lower repetition rates and rely on indirect detection of electrons. However, these experiments encounter limitations because they are required to use electron beams containing a relatively large number of electrons ($\gg 100$ electrons/pulse), leading to severe space-charge effects. Consequently, electron pulses with long durations and large transverse diameters are used to interrogate the sample. Here, we introduce a novel UED instrument operating at a high repetition rate and employing direct electron detection. We operate significantly below the severe space-charge regime by using electron beams containing 55 to 140 electrons per pulse at 30-kHz. We demonstrate the ability to detect time-resolved signals from thin film solid samples with a difference contrast signal, $\Delta I/I_0$, and an instrument response function as low as 10^{-5} and 243-fs (FWHM), respectively, without temporal compression. Overall, our findings underscore the importance of increasing the repetition rate of UED experiments and adopting a direct electron detection scheme. Our newly developed scheme enables more efficient and sensitive investigations of ultrafast dynamics in photoexcited samples using ultrashort electron beams.

I. INTRODUCTION

Ultrafast electron diffraction (UED)^{1–25} is a powerful technique that tracks changes in the position of atoms within a material in real-time with picometre and femtosecond spatio-temporal resolution. UED is often employed in pump-probe configuration where an optical (“pump”) pulse photoexcites a sample away from its ground-state structure and another, time-delayed, electron (“probe”) pulse measures diffraction patterns of the excited sample. Pulses of electrons with high kinetic energies (in the keV or MeV) are easily attainable, providing an electron probe pulse with a (sub-)picometre de Broglie wavelength^{26–28}. The Fourier transform of the resulting diffraction pattern yield structural information with a spatial resolution of less than 10-pm^{18,21,23,28}. Measurement of diffraction patterns at various time delays between the two pulses allows the retrieval of a real-space “movie” of structural changes in the excited sample during a photochemical reaction.

In the early 1980s, Mourou, Williamson and Li introduced the first picosecond variant of electron diffraction in transmission mode.^{1,2} The development of femtochemistry by Zewail^{29,30} enabled the use of femtosecond optical pulses to generate electron pulses^{31,3,7}. Despite this advancement, space-charge dispersion persisted in limiting the electron pulse duration to the picosecond regime.^{31,3,7} Following the groundbreaking contributions of Mourou^{1,2} and Zewail^{31,3,7}, extensive efforts have been dedicated to advancing the UED technique by numerous research groups and facilities. Figure 1 illustrates the impact of space-charge dispersion and the performance of different UED set-ups implementing diverse strategies. To reach a high spatio-temporal resolution, it is particularly important to generate an ultrashort electron pulse with the lowest pulse duration and transverse electron beam diameter. The electron pulse duration often dictates the total temporal resolution of UED measurements, referred to as the instrument response function (IRF). Reducing the transverse diameter of electron beams on-target minimizes the optical pump pulse diameter and, consequently, lowers the average power requirements of laser systems, which becomes particularly important when operating at high repetition rates. Furthermore, maintaining a high average beam current at the sample position is equally crucial to ensure the measurement of scattering signals with a high signal-to-noise (SNR) ratio. Realizing such optimal electron beam characteristics poses significant challenges owing to various constraints. These include limitations imposed by low repetition rates and severe space-charge effects, as well as issues associated with low electron scattering signals, non-optimal electron detection methodologies, and constraints related to electron beam flux and brightness.

The relatively low repetition rate of laser systems driving UED set-ups necessitates the use of electron pulses with relatively high bunch charges ($\gg 16$ -nC), leading to an increase in pulse duration from ~ 150 -fs to more than 1-ps in one metre propagation due to severe space-charge dispersion for keV electrons. In solid-state keV UED studies, space-charge effects were overcome by minimizing the sample-to-photocathode distance³², often to less than 5-cm, and improving the initial electron beam characteristics.^{33,34} This optimization yielded an IRF as short as 100 fs and transverse beam diameters as small as less than 100- μm .³³ However, instruments employing short sample-photocathode distances^{16,33,35–37} are generally incompatible with gas-phase UED experiments due to the higher operating pressures and the associated risk of voltage breakdown in the electron accelerator. So far, the generation

of ultrashort electron pulses with durations of 100 fs or less over longer electron propagation distances has become feasible through several advancements. These include the utilization of relativistic MeV beams^{9,13,14,17,20,21,38,39} or the implementation of temporal compression schemes employing radiofrequency (RF) fields generated by a microwave cavity^{40,10,41,42,19,43} or optical terahertz (THz) fields^{12,44–46}. Space-charge effects in 3-MeV electron beams are three orders-of-magnitude weaker than compared to <100-keV electrons at comparable bunch charge.¹³ This consequently enabled MeV-UED experiments with sub-150-fs time resolution.^{9,13,14,17,20,21,38,39} Notably, MeV-UED measurements with an IRF of sub-50-fs are now possible.¹⁷ However, access to accelerator-based MeV electron beams is confined to large-scale facilities, and achieving sub-10-fs time resolution with MeV set-ups necessitates precise synchronization of the RF accelerating field with the pump laser pulse^{20,25,41,47}. In keV UED instruments with a bunch charge much greater than 16-aC, the highest temporal resolution (FWHM) reported so far is approximately 100-fs in solid-state studies^{19,48,49} and 240-fs in gas-phase work¹⁵. Furthermore, notable achievements include temporal compression of single-electron pulses to 28-fs (FWHM)¹⁰ and the bunching of a 50-electron pulse into a train of 800-as single-electron pulses¹². However, employing UED instruments operating in low bunch charge mode (<16-aC)^{12,48,49} for gas-phase measurements will require laser systems with a higher repetition rate (≥ 100 -kHz) and average power (≥ 200 -W) than those currently employed.

Electron detection with a minimal noise contribution to the SNR ratio is another crucial factor. High-energy electron beams are often detected using a phosphor scintillator screen, which emits a few hundred photons for each detected electron.⁵⁰ The emitted photons are subsequently measured by either a fiber- or lens-coupled photon-sensitive imaging sensor. These sensors, which include charge-coupled device (CCD)⁵¹, electron-multiplying CCD (EMCCD)¹³, or complementary metal oxide semiconductor (CMOS)⁵⁰ technology, are susceptible to saturation effects from bright signals. For example, saturation from the unscattered beam is typically mitigated by employing a beam blocker positioned in-front of the phosphor screen. However, this approach results in the loss of valuable information on fluctuations in the electron beam's intensity and pointing, which are crucial for correcting these fluctuations. Furthermore, these charge-integrating analog detectors also suffer from relatively larger gain, integration and readout noise, limiting the SNR ratio that can be achieved.⁵⁰ Additionally, these indirect electron detection schemes often exhibit a limited dynamic range, particularly at high momentum transfers. It is worth noting that microchannel plates (MCPs), positioned in-front of a phosphor scintillator screen⁵¹, have also been used, however, their detection efficiency of high-energy electron beams (<15%) is not ideal.⁵²

In this work, we employ a novel, high repetition rate UED (HiRepUED) instrument operating at 30-kHz, utilizing direct electron detection. Our approach involves the use of temporally uncompressed electron pulses containing between 55 – 140 electrons, corresponding to a bunch charge of 8 – 24 aC. This bunch charge is significantly lower than that employed in existing (sub-)kHz UED set-ups (2-20 fC), leading to significantly weaker space-charge forces and lower emittances in keV beams, allowing us to operate in the low-to-moderate space-charge regime. We find that temporally uncompressed electron pulses as short as 235-fs are achievable, resulting in an IRF of ~243-fs. This IRF is similar to that reported for the keV UED instrument utilized by

Centurion and coworkers (240-fs) but using a compressed electron scheme¹⁵. Furthermore, we demonstrate the measurement of time-resolved signals with improved SNR ratio using direct electron detection as compared to indirect detection schemes. As a future outlook, we also discuss the future potential of our instrument with RF temporal compression, and give a brief discussion of its anticipated performance when operating in the ultrashort and ultrabright modes (see dashed lines in Fig. 1).

This paper is structured as follows. Details of the experimental set-up and simulations are given in Sections II and III, respectively. Results obtained from measurements and simulations are discussed in Section IV, and a summary conclusion is given in Section V.

II. EXPERIMENTAL

A. Optical set-up

Figure 2 shows a schematic of the optical set-up employed in this study. Here, the amplified output of a 30-kHz, 200- μ J laser system (Light Conversion PHAROS, 1025-nm, 6-W, 260-fs) was split into two beams using a half waveplate (HWP) and a thin film polarizer (TFP) positioned at Brewster's angle (see Fig. 2a). The *p*-polarized transmitted pulse was used as a supercontinuum seed pulse for white light supercontinuum generation (WLG) in the home-built optical parametric chirped-pulsed amplification (OPCPA) set-up. The *s*-polarized reflection was frequency converted to 512.5-nm (220-fs FWHM, 100- μ J) and was used as the pump beam of two non-collinear optical parametric amplification (NOPA) stages. The footprint of the OPCPA was 60 \times 45 cm². The signal output of the OPCPA ($\lambda_c = 800$ -nm, ~ 17 - μ J, ~ 190 -fs) was temporally compressed to 49 fs using prism compression (see Fig. 2b) close to its Fourier transform limit (TL) of 47-fs (19.5-nm FWHM bandwidth, see Fig. 2b). The compressed near-infrared (NIR) 800-nm pulse was split into two beams using an 80:20 beam splitter (see Fig. 2c) where one beam was used for electron generation while the second beam was used for sample photoexcitation.

In the electron generation (probe) beam, the NIR pulse (3- μ J) was frequency converted to 267-nm (20-nJ, 90-fs, TL: 42-fs) using a compact third harmonic generation unit (Eksma Optics, FemtoKit) composed of two BBO crystals, a HWP and a calcite plate (CP). Two harmonic separating dichroic mirrors (DMs) separated the 267-nm ultraviolet (UV) pulse from the residual 400-nm and 800-nm pulses. The UV pulse was subsequently beam expanded using two curved mirrors (CMs) by a magnification factor of two, producing a collimated UV beam (~ 5 -mm FWHM diameter). The UV pulse was then power attenuated using a HWP and TFP positioned at Brewster's angle. The *p*-polarized transmitted pulse was used for UV pulse diagnostics and alignment purposes. The *s*-polarized reflection was directed to the UED instrument, where it was focussed to a 30- μ m FWHM diameter spot on the photocathode (see beam profile in Fig. 2d). The ultraviolet (UV) pulse duration at the photocathode was estimated to be 90-fs based on the group dispersion delay (GDD; ~ 1200 -fs²) expected from the UV optics employed in our optical set-up (see Fig. 2b). The pointing stability of the UV pulse at the focus was measured to be ~ 0.50 - μ m using a UV-sensitive beam profiling camera (PCO.edge 4.2 bi UV) over a ~ 15 -minute period, as shown in Fig. 2e-h. Additionally, an intensity jitter of 1% (FWHM) was observed

during this period. As the UV pulse is generated through non-linear conversion using an 800-nm pulse, the above-mentioned jitter values of the UV pulse can be taken as the maximum corresponding values for the 800-nm pulse. Notably, our optical setup does not employ a beam pointing stabilization system.

In the sample photoexcitation (pump) beam, the NIR pulse energy (12- μ J) was attenuated using a HWP and TFP at Brewster's angle, and subsequently reflected by a retroreflector mounted on a linear delay stage (Physik Instrumente M-531.2S1, 30-cm travel range). The NIR pulse was beam expanded and subsequently focussed to a \sim 180- μ m diameter spot at the sample position using a plano-convex uncoated lens ($f = +600$ -mm). The relative angle of the optical pump pulse to the electron axis was \sim 20°. The mirror after the NIR lens and the last mirror before the sample are piezo-mounted to obtain the optimal spatial overlap with the electron beam at the sample position.

B. Experimental set-up

Figure 3 shows a schematic of the HiRep-UED instrument employed in this study. The UV pulse was focussed to a 30- μ m FWHM diameter spot (see Fig. 2d) on a high purity oxygen-free copper photocathode (>99.99%)⁵³. Since the photocathode was held at a high voltage of 95-keV with a high voltage power supply (Matsusada AU-100N1.5-L), the effective work function of copper was reduced due to the Schottky effect (\sim 4.3-eV)⁵³ such that the photon energy of the UV pulse (4.61-eV) was sufficiently high to generate electrons via photoemission. A grounded anode flange positioned \sim 11-mm away from the photocathode generated a constant direct current (DC) field with a field strength of $E_{DC} < 10$ MV/m, sufficient to accelerate the electron beam to 95-keV. The electron beam passed through a 10-mm aperture and was transversely collimated and focussed by two solenoid magnetic lenses (MLs) labelled ML1 and ML2, respectively. The collimating solenoid magnetic lens ML1 (Doctor X Works) was placed directly in front of the anode flange located 40 mm away from the photocathode. ML1 consisted of rectangular (2.5 x 1.5 mm) copper wire wound into a coil with 351 turns, an inner and outer diameter of 42.5-mm and 68.5-mm, respectively, and a length of 60-mm. The condensing solenoid magnetic lens ML2 (Doctor X Works) was placed \sim 670-mm away from the photocathode. ML2 comprised of circular (1-mm diameter) copper wire wound with 650 turns forming a 60-mm length coil with an inner and outer radius of 20-mm and 37.5-mm, respectively. The centre hole is 35-mm in diameter. A maximum on-axis magnetic field flux density of 40-mT (17.5-mT) at 12 A (1.75 A) for ML1 (ML2) can be generated. The focussed electron beam scattered against thin-film solid-state samples held by a 0.5-mm thick copper block capable of holding up to nine samples with 3-mm diameter. The sample holder was mounted onto a manual four-axis (x, y, z, θ_{yaw}) ultrahigh vacuum mechanical translator stage (VAb Vakuum-Anlagenbau). A radiofrequency (RF) microwave cavity (Doctor X Works) for temporal electron compression was installed together with an active synchronization system that corrects the RF-laser timing jitter based on Ref.⁴¹. However, both are unused in this work as it is beyond the scope of the current work and is subject of a separate publication.

The scattered and unscattered electrons are measured with a direct electron detector (DECTRIS QUADRO)^{54,55} composed of 512×512 pixels with $75 \mu\text{m} \times 75 \mu\text{m}$ size, giving a total active area of $38.4 \text{ mm} \times 38.4 \text{ mm}$. Each pixel was composed of a 450-

μm thin silicon wafer integrated with additional thin layers of GdTe and GaAs, each less than 100-nm thick. This combination ensures a detection efficiency of more than 90% for 95-keV electrons (*i.e.*, single-electron detection). Each pixel can detect up to four electrons per pulse (see Section IV.B), while possessing a 32-bit dynamic detection range (sum of two 16-bit electron counters), capable of counting up to 4.2×10^9 hits in a given exposure time. The detector's maximum count rate was determined as 10^7 electrons/second/pixel under continuous illumination.⁵⁴ Loss of sensitivity was observed with the detection of an unfocussed electron beam containing more than 10^4 electrons at 30-kHz, with the beam covering the full sensor dimensions. In addition to the electron detector, a home-built Faraday cup (not shown in Fig. 3; 2-mm open aperture diameter, 20-mm length) positioned in-front of the detector was used to measure the average current of the electron beam containing more than 10^4 electrons. Practical acquisition times for time-resolved measurements at 30-kHz spanned from between 20 to 90 minutes for data shown in this work. Typical instrument parameters of the HiRep-UED set-up are summarized in Table I. Further details of the HiRep-UED instrument are provided in Section S1B of the Supplementary Information.

Table I. Typical machine parameters for the HiRep-UED set-up in this work.

Parameters	Values
Repetition rate	30-kHz
Vacuum in the following chambers	
Electron accelerator	$<7\text{E-}7$ mbar
RF cavity	$<3\text{E-}8$ mbar
Sample chamber	$<3\text{E-}8$ mbar
Electron beam kinetic energy	95-keV
Electron beam charge	8.8-aC to 22-aC (55 - 140 electrons/pulse); overall range is 1.6-aC to 1.6-pC (<i>i.e.</i> , 1 to 10^6 electrons/pulse)
Electron flux	1.5×10^6 to 4.2×10^6 electrons/second, (maximum of 3.0×10^{10} electrons/second)
At the photocathode position	
UV pulse size (FWHM)	30- μm
UV pulse duration (FWHM)	90-fs (TL: 42-fs)
UV pulse energy	<20 -pJ (overall range of 1-pJ to 20-nJ)
At the sample position	
Electron beam charge (after passing through aperture)	1.4-aC to 6.8-aC (9 to 42 electrons/pulse)
Electron bunch length (FWHM)	235-fs to 322-fs (uncompressed), (<50 -fs compressed predicted by GPT)
Electron beam size (FWHM)	~ 100 - μm (200- μm)
Electron beam transverse pointing jitter (FWHM)	≤ 28 - μm
Transverse coherence length (RMS)	3.8-nm
Transverse emittance (RMS)	5.6 nm·rad
Longitudinal emittance (RMS)	103 fm·rad to 177 fm·rad
Pump laser spot size (FWHM)	~ 180 - μm
Pump laser duration (FWHM)	<60 -fs (TL: 47-fs)
At the detector position	
Electron beam size (FWHM)	~ 450 - μm (280- μm)

Reciprocal-space resolution	0.063-Å ⁻¹
Spatial resolution	3.8-µm

III. SIMULATIONS

A. General Particle Tracer simulations

General Particle Tracer (GPT) simulations of the UED instrument were performed using an electron beam with a kinetic energy of 95-keV, and an excess thermal energy of 0.5-eV. The electron beam was generated by a UV pulse with a FWHM diameter and duration of 30-µm and 90-fs, respectively, without the use of the RF cavity (*i.e.*, temporally uncompressed mode). For comparison, simulations were also performed with RF-compressed electron beams (*i.e.*, temporally compressed mode), using a UV pulse duration of 60-fs. Field maps of the electron accelerator and solenoid magnetic lenses, generated from finite element method (FEM) simulations, were used. For each simulation, we used 10,000 macroparticles with the mesh method.

IV. RESULTS AND DISCUSSIONS

A. Electron beam characterization

1. Electron flux

Our UED set-up is capable of generating an electron pulse containing between one and $>10^6$ electrons at 30-kHz with a UV pulse energy between ~ 1 -pJ to 20-nJ, as shown in Fig. 4a. Operating in high-brightness mode, our setup achieves an unprecedented electron flux exceeding 10^{10} electrons/second, surpassing existing keV-scale UED systems by more than an order of magnitude^{15,19,22,25,42}. Compared to the brightest MeV-scale UED set-up,¹³ our system has a 100-fold higher electron flux. Considering the factor of four higher elastic electron scattering cross-section for 95-keV electrons compared to 3-MeV electrons, calculated with ELSEPA,⁵⁶ the maximum electron scattering signal from our set-up is approximately 400 times greater than the current state-of-the-art in MeV-UED¹³. Even in anticipation of upgrades to MeV-UED facilities aiming for a 1-kHz repetition rate, the difference in signal level between our setup and MeV-UED remains appreciably high (factor of ~ 150).

2. Electron transverse profile at sample and detector

We performed measurements to determine the full-width at half-maximum (FWHM) diameter of an electron beam containing 100 electrons. Using specific combinations of ML1 and ML2 currents, we adjusted the transverse focus of the beam to be positioned either close to the sample or the detector. Knife-edge scans were employed to measure the electron beam size at the sample position. The electron beam size at the detector was measured directly on the direct electron detector. In our typical operating configuration, with the transverse focus at the sample, we measured beam diameters of 102-µm and 453-µm at the sample and the detector, respectively (see Fig. 4b-c). With a different combination of ML1 and ML2 currents, we were able to reduce the electron beam diameter to approximately 280-µm at the detector, albeit with a larger 200-µm diameter at the sample. Figure 3b shows corresponding General Particle Tracer (GPT) simulations of the transverse diameter of an electron pulse

containing 55 electrons in our UED instrument (*i.e.*, 8.8-aC; see red line). The initially divergent electron beam is collimated by ML1 to a diameter of 450- μm (FWHM) at the position of the RF cavity ($\sim 0.5\text{-m}$ from photocathode). The collimated beam is subsequently focussed by ML2 to 100- μm (FWHM) close to the sample position ($\sim 0.95\text{-m}$ from photocathode). A good agreement between the measured (102- μm) and simulated (100- μm) transverse beam diameter at the sample position is observed. This operational mode places our instrument in the low-to-moderate space-charge regime. The GPT simulations further predict an RMS transverse and longitudinal emittance at the sample of 5.6 nm·rad and 103 fm·rad (10.5 nm·rad and 11.4 pm·rad), respectively, for a bunch charge of 8.8-aC (16-fC).

3. Reciprocal-space resolution and transverse coherence length

The reciprocal-space resolution and transverse coherence length of our instrument were characterized experimentally by measuring the electron diffraction pattern from a monocrystalline gold film (Plano GmbH, 11-nm) and a polycrystalline aluminium film (Plano GmbH, 31-nm) using a 95-keV electron pulse containing ~ 100 electrons on-target. These reference samples are often used to characterise both gas-phase and solid-state UED instruments. Fig. 5a shows distinct Bragg diffraction spots from the monocrystalline film. Our instrument was further characterized for isotropic electron diffraction signals, which are typically measured in gas-phase UED, by measuring the diffraction pattern generated from the polycrystalline film, as shown in Fig. 5b. From the FWHM of the first-order diffraction peaks, we obtain a reciprocal-space of 0.063 \AA^{-1} . An excellent agreement is observed between measured and simulated data, the latter of which is calculated using a powder electron diffraction simulation software (CrystalMaker[®])⁵⁷. Furthermore, the RMS transverse coherence length, ϵ_{co} , of our UED instrument was experimentally characterized using the method described in Ref.¹¹ that takes into account the reciprocal-space RMS widths of and distance between two closely-lying Bragg electron diffraction signals. Here, we used the electron diffraction signals corresponding to the $(hkl) = (220)$ and (420) Bragg peaks in gold monocrystalline film and the $(hkl) = (220)$ and (311) peaks in polycrystalline aluminium. We obtain a ϵ_{co} value of 3.8-nm from both data.

4. Electron pulse pointing and intensity jitter

Fig. 6 shows the long-term pointing and intensity drift of the electron beam measured with a direct electron detector over a two-hour period. The beam pointing and intensity fluctuations of the electron beam were characterized experimentally (see Fig. 6d-f). A Gaussian fit to the histogram distribution of electron intensity in Fig. 6d shows that the electron beam has a 5% (FWHM) intensity fluctuation. While a horizontal and vertical pointing jitter of 23- μm and 28- μm , respectively, are observed (see Fig. 6e-f).

5. Comparison to other UED instruments

The transverse diameter and reciprocal-space resolution of the electron beam in our instrument is a factor of two-to-three smaller than other instruments employing bunch charges exceeding 8.8-aC^{13,15,19,42}. This reduction is attributed to a lower transverse emittance enabled by the use of an electron beam with a reduced bunch charge (8.8-aC). Notably, the transverse emittance at 8.8-aC (5.6 nm·rad) is nearly a factor of two smaller than that reported for other instruments typically operating at 16-fC (10

nm·rad)^{22,23,58}. Moreover, the larger RMS transverse coherence length, ϵ_{co} , of our UED instrument (3.8-nm) compared to the state-of-the-art (~ 3 -nm)^{11,13,59} has important implications for coherently imaging larger lattice unit cell and molecular structures. For example, for solid-state samples, a larger ϵ_{co} would mean that the lattice unit cell could be probed an additional number of times, improving the signal-to-noise ratio of the measured electron diffraction signal. Furthermore, the pointing stability of our instrument (≤ 28 - μm) is similar to that reported for the MeV-UED instrument at SLAC (33- μm)¹³.

B. Direct electron detection

1. Saturation effects in a direct electron detector

Figure 7a shows detector images of the unscattered electron beam containing a varied number of electrons, from 10 electrons/pulse to more than 4100 electrons/pulse, recorded after passing through a monocrystalline 11-nm gold thin film sample. Saturation effects become apparent using an electron pulse containing 134 electrons (see Fig. 7a4). For example, the vertical profile of the electron beam (see Fig. 7d) is modified from a Gaussian distribution below saturation to a bimodal distribution when the central pixels become saturated by an electron beam containing 134 electrons or more. Furthermore, in the case of more than 4100 electrons/pulse (see Fig. 7a8), significant saturation effects occur; the central pixels detecting the central portion of the electron beam deviate from a normal counting detector behaviour. We note nevertheless that when the central pixels of the detector are saturated by the unscattered electron beam, the scattered signal observed at larger radii on the detector is not affected, as shown in Fig. 7i. This demonstrates that every pixel operates as an independent electron counter. This is in contrast to the typically-employed CCD⁵¹, EMCCD¹³, and CMOS⁵⁰ detectors.

Furthermore, with an exposure time of 33- μs (i.e., 1 shot), the radial distribution of an electron beam containing 100 electrons is measured with a high SNR ratio. While an exposure time of at least 3.33-ms is required to measure the first-order (200) and (220) Bragg diffraction peaks of monocrystalline gold with a SNR ratio of four (see Fig. 7h). Measurement of electron signals significantly above the pixel saturation threshold (see Fig. 7f) reveals that the corresponding pixels behave like a paralyzed counting detector,⁶⁰ with signal decreasing as exposure time increases from 33.3- μs to 3.0-ms. Moreover, a sudden intensity surge is observed at an exposure time of 30.0-ms, followed by a decline in signal at longer exposure times. Given the presence of two 16-bit counters in each pixel, this observed saturation behaviour is attributed to the initial paralysis of the first 16-bit counter, followed by the subsequent paralysis of the second 16-bit counter. Notably, in this regime, an exposure time of 33.3- μs (i.e., a single shot) is sufficient to measure the first-order diffraction peaks with an SNR ratio of four (see Fig. 7i), demonstrating the high sensitivity of this detector.

Specifically, each pixel of this detector utilizes a retrigger mechanism which counts the length in time that the amplitude of the measured signal is above a predefined value corresponding to a threshold energy (in our case 12-keV). This length in time is measured as multiples of a programmable time, called the retrigger time (i.e., the time that the signal from one electron is above threshold). The amplitude of the signal is approximately proportional to the energy deposited by the 95-keV electron in that pixel.

Therefore, when multiple electrons impinge on the same pixel, this generates a signal with an amplitude that is the sum of the energy deposited by each electron. At every retrigger time that the signal is still above threshold, a count is added to the electron counter. Thus, longer time-over-threshold durations enable the QUADRO to distinguish multiple hits from a single hit.^{54,61} Under continuous illumination, a limit of 10^7 electrons/second/pixel with a retrigger time of 10-ns was established.⁵⁴ In our pulsed operation, conducted below saturation, our analysis from Fig. 7d-e indicates that approximately three electrons per pulse can be detected by a single pixel (*i.e.*, 9×10^4 electrons/second/pixel, and a retrigger time of 825-ns). Thus, the QUADRO's retrigger feature enables the counting of up to three electrons arriving within the electron pulse duration (<350-fs) in a single pixel at 30-kHz.

2. Shot-to-shot jitters and their correction

We have characterized the electron beam's intensity and pointing fluctuations on a shot-to-shot basis. To demonstrate the capability to correct for such fluctuations, we performed measurements immediately after applying current to the two magnetic solenoid lenses, without allowing time for thermalisation, to ensure maximum fluctuation in the electron beam. Employing a similar histogram analysis as that presented earlier, we find that an electron beam containing 113 electrons exhibited a FWHM intensity jitter of 25.7 electrons or 22.7%. This is approximately equivalent to the shot noise limit assuming Poisson statistics ($\sim 22.2\%$)⁵⁰. Furthermore, changes in the electron beam's centre position, Δx and Δy , were 56- μm and 75- μm , respectively.

An algorithm was developed that implements multiple corrections on a shot-to-shot basis, applicable to data measured with any direct electron detector. Initially, each element within the 512×512 pixel matrix of every image was normalised by the total number of electrons present in the unscattered beam. The resulting sum detector image before and after intensity correction is shown in Fig. 9a and 9b, respectively. Exploiting the ability to bin Δx and Δy into 0.1-pixel bins (see histograms at top of Fig. 8b-c), the dimensions of the detector image were expanded from the original 512×512 pixels to 5120×5120 pixels by sub-dividing each pixel into a 10×10 grid. This is referred to as the sub-pixelation method. Each element within this 10×10 pixel array retained the same intensity value as its corresponding original pixel. Changes in centre positions were corrected on a shot-to-shot basis with 0.1-pixel precision of the original 512×512 pixel matrix, utilizing the newly formed 5120×5120 pixel matrix. The resulting sum detector image of the fully corrected electron beam is depicted in Fig. 9c. The normalised radial distributions before and after correction are presented in Fig. 9d-f for both unscattered and scattered electrons. It is evident that a more uniform unscattered electron beam is achieved after full correction (blue line in Fig. 9d) compared to the intensity-only corrected data (red line) and the uncorrected data (black line). Notably, oscillations in the fully corrected signal (see Fig. 9d) are due to aliasing effects arising from the use of 0.1-pixel bin sizes during the sub-pixelation process. Moreover, the shoulder observed for the (220) Bragg peak in the uncorrected data is no longer present in the fully corrected dataset (see grey shaded area in Fig. 9e). Such a shot-to-shot correction offers the capability to correct measured scattering data despite intensity and pointing fluctuations in the primary electron beam. This capability has not been attainable thus far in UED instruments utilizing other types of electron detectors mentioned previously. In the subsequent section, the efficacy of correcting the electron beam intensity jitter is demonstrated.

C. Time-overlap between optical-pump and electron-probe

We investigate the time-resolved pump-probe capability of our UED instrument through space-charge deflection of the primary electron beam (235-fs FWHM, 55 electrons/pulse, 100- μm FWHM diameter at sample) by photoelectrons generated at the surface of a meshgrid (300 lines/inch).¹¹ Figure 10a displays detector images of the electron beam measured at various pump-probe delays. The green circled area highlights significant, time-resolved changes in the measured electron counts attributed to space-charge vertical deflection of the electron beam. This is particularly evident at 12.5-ps. To quantify the measured time-resolved signal, we integrate the electron counts in each row of y -pixels across all x -pixels, effectively creating a horizontal strip detector (depicted by blue rectangles in Fig. 10a at the delay of -15 ps). For each pump-probe delay (Δt), we subtract the pump-probe signal (I_{pp} ; see Fig. 10b) by a reference probe-only signal (I_0) which provides the difference electron signal (ΔI ; see Fig. 10c). The I_0 signal is a single image generated from the average of all images measured at negative Δt values. Figures 10b-c reveal a substantial increase in electron counts along the $y = 326$ pixel row strip line (see green lines). This is accompanied by a decrease in signal along the $y = 328$ pixel row (see light-blue lines) in the first 13-ps after t_0 . These variations in electron signal correspond to the vertical deflection of the electron beam by photoelectrons, returning to its original position by 65 ps.

Figure 11a illustrates the fluence dependence of the time-resolved difference contrast signal, $\Delta I/I_0$, arising from space-charge deflection. We define a circular region of interest (ROI) with a radius of four pixels that is centred on the electron beam. On a pixel-by-pixel basis, and at each pump-probe step, we normalise the difference electron signal, ΔI , by the sum of the electron beam to correct for fluctuations in the electron beam intensity. The ΔI signal in each pixel of the ROI is further normalised by I_0 to derive the difference contrast signal, $\Delta I/I_0$. A minimum fluence of $\sim 18 \text{ mJ/cm}^2$ is necessary to detect a discernible $\Delta I/I_0$ signal. As the fluence increases, so does the $\Delta I/I_0$ signal, reaching up to 0.03 (*i.e.*, a 3% change relative to the probe-only signal) with a fluence of 65 mJ/cm^2 .

In our investigation, we also study the influence of the electron beam's transverse diameter at the sample position on the measured $\Delta I/I_0$ signal. Figure 11b shows measurements conducted with two different electron beam FWHM diameters: 102- μm (solid lines) and 200- μm (dashed lines). In both cases, increasing the number of electrons passing through the 100- μm aperture placed in-front of the meshgrid leads to an increase in the $\Delta I/I_0$ signal. However, employing a smaller electron beam diameter at the sample yields a $\Delta I/I_0$ signal with approximately 50% higher contrast. Our results complement previous studies utilizing similar space-charge deflection techniques. Previous investigations often utilized electron beams in either shadow imaging mode^{62,63}, characterized by a notably larger beam diameter at the sample, or in an intermediary mode between shadow and reciprocal-space imaging, utilizing a moderately large beam diameter. Our study demonstrates that achieving a significant $\Delta I/I_0$ signal is equally feasible in reciprocal-space imaging mode. This is accomplished by employing an electron beam with the smallest FWHM diameter, which in our case was equivalent to the aperture's inner diameter. The inset of Fig. 11b shows the absolute difference contrast signal, $|\Delta I/I_0|$, at negative pump-probe

delays, where its average (standard deviation) value is 7×10^{-5} (6×10^{-5}). This represents a 27-fold reduction compared to the minimum $\Delta I/I_0$ measurable with EMCCD detection using the MeV-UED instrument at SLAC (2×10^{-3} or 0.2%). The SNR ratio observed in Fig. 11b ranges from 140 to 70, which starkly contrasts the SNR ratio of 5 to 2.5 typically obtained with EMCCD detection¹³. The significant disparity in SNR ratios emphasizes the critical importance of acquiring electron signals with minimal noise, which is inherently possible with direct electron detection. For example, the in-pixel digital counting capability of a direct electron detector minimizes inherent sources of noise in the pixel (e.g., gain, integration operations) and readout electronics which have often limited the SNR ratio in charge-integrating analog detectors,⁵⁵ such as CCD and CMOS sensors. Our HiRep-UED instrument employing direct electron detection is primarily limited by shot noise⁵⁰, arising from the measured signal statistics, and source noise⁵⁰, resulting from fluctuations in the electron beam.

D. Time-resolved dynamics in photoexcited aluminium thin film measured with high sensitivity

We next demonstrate the ability to measure relatively weak time-resolved elastic electron scattering signals from a photoexcited sample that is beyond the detection sensitivity of most existing UED setups. To demonstrate this detection sensitivity, we utilize a 31-nm thin film of polycrystalline aluminium as a prototypical system. The aluminium sample is optically excited with an 800-nm pulse (<60-fs FWHM, ~180- μ m FWHM diameter, 1 mJ/cm²) and probed by a 95-keV electron pulse containing 140 electrons (322-fs FWHM, ~100- μ m FWHM diameter). Fig. 12 shows the $\Delta I/I_0$ signal of the (331) diffraction peak before (black squares) and after (red circles) correcting for fluctuations in the electron beam intensity at each pump-probe step. In both cases, we observe a step-function decrease in the $\Delta I/I_0$ signal with a fall time of 9.4-ps (FWHM), attributed to the thermal Debye-Waller effect^{64,65}. Additionally, the decreasing signal exhibits sinusoidal oscillations with a period of 7.25 ± 0.25 ps, reaching a constant $\Delta I/I_0$ value at 45 ps. These oscillations are attributed to a coherent acoustic phonon mode resulting from sound propagating along the longitudinal direction of the sample.⁶⁴⁻⁶⁶ The measured oscillation period of 7.25 ± 0.25 ps for our 31-nm thick aluminium sample is in agreement with reported data for thinner samples⁶⁶. In these thinner samples, the period of acoustic phonon modes has been reported to increase from 3.8-ps to 6.4-ps with increasing sample thickness from 10 ± 3 nm to 20 ± 3 nm.⁶⁶ Furthermore, the importance of correcting for fluctuations in the electron signal intensity becomes evident between 36 ps and 44 ps (see grey shaded area). A rapid decrease in signal at 38-ps observed in the raw data disappears in the normalised data, with the standard deviation in signal between 36 – 44 ps decreasing by a factor of 2.5 to 4×10^{-6} after normalisation. At negative delays, the average (standard deviation) value of $|\Delta I/I_0|$ is 3×10^{-6} (2×10^{-6}). These findings underscore the high sensitivity of our direct electron detection system, which is more than two orders of magnitude more sensitive than indirect electron detection schemes employed in other UED instruments.

E. Simulation of temporal compression in the HiRep-UED instrument

In this work so far, we have utilized an electron pulse without temporal compression. However, ongoing efforts are directed towards achieving temporal compression of the electron pulse using an RF compression scheme. While the RF compression of our

electron pulse is subject to a future publication, it is still pertinent to explore the anticipated capabilities of our instrument when employing RF-compressed electron beams. Fig. 13 shows the FWHM pulse duration and transverse beam diameter at the sample position predicted by GPT simulations for an RF-compressed (red squares) and uncompressed (black circles) electron beam containing from one to 10^7 electrons. Here, a UV pulse duration of 60-fs (90-fs) FWHM was used in the simulations with (without) RF-compression. The simulations show three distinct regimes of space-charge effects across the single-electron to single-shot operating regimes: no-to-low space-charge (regime I; green shaded), low-to-moderate space-charge (regime II; blue shaded), and severe space-charge (regime III). By implementing RF compression in our instrument, we can achieve pulse durations of 50-fs or less (see dashed line in Fig. 13a) with electron beams containing 250 electrons or fewer, as predicted by GPT simulations. This represents a more than tenfold reduction in pulse duration compared to uncompressed electron beams with the same bunch charge. Furthermore, utilizing electron beams containing 250 electrons at 30-kHz results in an electron flux of 7.5×10^6 electrons/second, which is more than two times higher than that of the MeV-UED instrument at SLAC operating at 0.36-kHz¹³. The predicted 50-fs compressed pulse duration would be over two (nearly four) times shorter than that of the MeV-UED instrument at SLAC¹³ (keV-UED set-up in Ref.¹⁵). Such a short pulse would enable imaging of nuclear dynamics in gas-phase photochemical reactions that reach completion in less than 500-fs,⁶⁷⁻⁶⁹ which have thus far been too rapid to image with existing UED instruments. Moreover, ensuring a minimal transverse diameter of the electron is also crucial to minimize the pump pulse diameter and average power requirements of the laser system operating at high repetition rates. With RF compression, it is anticipated that an electron beam diameter of 100- μm (see dashed line in Fig. 13b) could be achieved with a beam containing 500 electrons. In general, GPT simulations predict that electron beams containing 1 - 10^7 electrons will exhibit compressed (uncompressed) pulse durations of 9 fs – 283 fs (174 fs – 14 ps) and transverse diameters of 44 μm – 282 μm (102 μm – 787 μm). Figure 1 illustrates the range of operating parameters anticipated for our instrument based on GPT simulations (see red dashed lines). These operating regimes are broadly categorized as the ultrashort and high brightness modes. The ultrashort mode is projected to achieve pulse durations of 50-fs or less, while the high brightness mode is capable of pulse durations of below 300 fs but with a substantially higher average current of nearly 70-nA. This average beam current surpasses that of the brightness existing ultrashort keV^{42,70} (MeV^{13,17}) electron beam sources by more than one (four) order(s) of magnitude.

V. CONCLUSIONS

In summary, we introduce a novel high repetition rate UED (HiRep-UED) instrument operating at 30-kHz with direct electron detection. We demonstrate the feasibility of operating in the low-to-moderate space-charge regime at 30-kHz, enabling the acquisition of statistically significant electron signals within a reasonable acquisition time of up to 90 minutes. Within this regime, the electron beam exhibits relatively low transverse and longitudinal emittance, facilitating the use of temporally uncompressed electron pulses containing 55-140 electrons. This setup allows the measurement of time-resolved signals from photoexcited samples with an instrument response function as low as ~243-fs (FWHM). Additionally, transverse focussing of the electron beam to a spot diameter as small as ~100- μm (FWHM) is possible at the sample position. By

employing direct electron detection, we demonstrate the ability to measure time-resolved effects in thin film aluminium with a difference contrast $\Delta I/I_0$ signal on the 10^{-5} order of magnitude. This high detection sensitivity is made possible by the direct detection of electrons with reduced noise associated with pixel (e.g., gain, integration operations) and readout electronics. Furthermore, direct electron detection enables the measurement of the unscattered primary electron beam, a capability that proves invaluable in correcting for fluctuations in the electron beam's intensity through our experiments under varied experimental conditions.

Our ongoing efforts to improve our setup include the implementation of temporal compression of our electron beam using RF fields generated by a microwave cavity. Firstly, the UV pulse will be chirp-compensated to sub-60-fs using chirped mirrors, suitable for the UV range, possessing negative GDD. Furthermore, the installation of this cavity is complete, and work is currently underway to optimize its functionality. Additionally, we have implemented an active RF-laser synchronization system based on Ref.⁴¹ to correct fluctuations in the RF-laser timing jitter. The implementation of RF compression into our setup is predicted to extend our capabilities, offering a compressed electron beam with variable duration (9 fs to 283 fs) and average current (5-fA to 50-nA). This broad operational range will enable our setup to operate in or between ultrashort and ultrabright modes, catering to diverse experimental requirements.

Future iterations of UED setups could benefit from several enhancements. One avenue for improvement involves minimizing the excess transverse momentum spread and thereby reducing the transverse emittance of the electron beam. This would then further reduce the transverse electron beam diameter at the sample position. This could be achieved by adopting new photocathode materials with lower work functions^{22,71} than traditional options like copper⁵³ and gold³³. Moreover, this would enable the use of visible optical pulse in electron photoemission^{34,71}, allowing to match the photocathode work function³⁴, resulting in the generation of photoelectrons with minimal excess energy and lower emittance. This approach, facilitated by ultrashort visible pulses, represents a highly desired departure from the commonly used ultraviolet pulses.

Furthermore, our system's current repetition rate of 30-kHz is already well-placed for gas-phase UED measurements planned in the near future. However, scaling the repetition rate of the system to, for example, 100-kHz is feasible using currently available high-average power, femtosecond laser systems. Given that the average power and repetition rate of femtosecond laser systems have continually increased over the last three decades, scaling to hundreds of kHz (or even to the MHz level) is conceivable in the future. Increasing the repetition rate would offer significant benefits, including the ability to utilize electron beams with lower bunch charges. Gas-phase UED measurements could then utilize electron beams experiencing no-to-low space-charge dispersion^{10,12,44,48} and optimal emittance properties but at the hundreds of kHz or 1-MHz repetition rate, particularly when combined with direct electron detection. Additionally, ultrashort electron beams with optimal emittance properties offer promising applications in other areas, such as electron energy loss spectroscopy^{23,72} with the use of streaking fields⁷³⁻⁷⁵, dipole magnets^{76,77} and monochromation techniques⁷⁸.

ACKNOWLEDGEMENTS

The authors are grateful for fruitful discussions and valuable support provided by Arnaud Rouzée, Brad Siwick, Jom Luiten, Christoph Reiter, Roman Peslin, Wolfgang Krueger, Rainer Schumann, Octave Grob, Tancrede Esnouf, Laurenz Kremeyer, Alexander Hume Reid, and Ming-Fu Lin. We thank DECTRIS (Luca Piazza, Pietro Zambon) for the provision of the QUADRO direct electron detector and valuable discussions. We thank DrXWorks (Jim Franssen, Thomas Luiten), Pulsar Technologies (Bas van der Geer, Marieke de Loos), Light Conversion (Ignas Abromavičius, Valdas Maslinkas) and TOPAG (Hannes Stroebel, Igor Quint) for extensive support. The authors are also grateful for financial support from Max-Born-Institut.

DATA AVAILABILITY

The data that support the findings of this study are available from the corresponding author upon reasonable request.

REFERENCES

- ¹ G. Mourou, and S. Williamson, "Picosecond electron diffraction," *Appl. Phys. Lett.* **41**(1), 44–45 (1982).
- ² S. Williamson, G. Mourou, and J.C.M. Li, "Time-resolved laser-induced phase transformation in aluminum," *Phys. Rev. Lett.* **52**(26), 2364–2367 (1984).
- ³ J.C. Williamson, J. Cao, H. Ihee, H. Frey, and A.H. Zewail, "Clocking transient chemical changes by ultrafast electron diffraction," *Nature* **386**(6621), 159–162 (1997).
- ⁴ H. Ihee, J. Cao, and A.H. Zewail, "Ultrafast electron diffraction: structures in dissociation dynamics of Fe(CO)₅," *Chem. Phys. Lett.* **281**(1), 10–19 (1997).
- ⁵ J. Cao, H. Ihee, and A.H. Zewail, "Ultrafast electron diffraction: determination of radical structure with picosecond time resolution," *Chem. Phys. Lett.* **290**(1), 1–8 (1998).
- ⁶ J. Cao, H. Ihee, and A.H. Zewail, "Ultrafast electron diffraction and direct observation of transient structures in a chemical reaction," *Procl. Natl. Acad. Sci. U.S.A.* **96**(2), 338–342 (1999).
- ⁷ H. Ihee, V.A. Lobastov, U.M. Gomez, B.M. Goodson, R. Srinivasan, C.-Y. Ruan, and A.H. Zewail, "Direct imaging of transient molecular structures with ultrafast diffraction," *Science* **291**(5503), 458–462 (2001).
- ⁸ R.J.D. Miller, "Femtosecond crystallography with ultrabright electrons and X-rays: Capturing chemistry in action," *Science* **343**(6175), 1108–1116 (2014).
- ⁹ P. Zhu, Y. Zhu, Y. Hidaka, L. Wu, J. Cao, H. Berger, J. Geck, R. Kraus, S. Pjetrov, Y. Shen, and others, "Femtosecond time-resolved MeV electron diffraction," *New. J. Phys.* **17**(6), 063004 (2015).
- ¹⁰ A. Gliserin, M. Walbran, F. Krausz, and P. Baum, "Sub-phonon-period compression of electron pulses for atomic diffraction," *Nat. Commun.* **6**(1), 8723 (2015).
- ¹¹ D.S. Badali, R.Y.N. Gengler, and R.J.D. Miller, "Ultrafast electron diffraction optimized for studying structural dynamics in thin films and monolayers," *Struct. Dyn.* **3**(3), 034302 (2016).
- ¹² Y. Morimoto, and P. Baum, "Diffraction and microscopy with attosecond electron pulse trains," *Nat. Phys.* **14**(3), 252–256 (2018).

- ¹³ X. Shen, J.P.F. Nunes, J. Yang, R.K. Jobe, R.K. Li, M.-F. Lin, B. Moore, M. Niebuhr, S.P. Weathersby, T.J.A. Wolf, C. Yoneda, M. Guehr, M. Centurion, and X.J. Wang, “Femtosecond gas-phase mega-electron-volt ultrafast electron diffraction,” *Struct. Dyn.* **6**(5), 054305 (2019).
- ¹⁴ J. Yang, X. Zhu, J.P.F. Nunes, K.Y. Jimmy, R.M. Parrish, T.J. Wolf, M. Centurion, M. Gühr, R. Li, and Y. Liu, “Simultaneous observation of nuclear and electronic dynamics by ultrafast electron diffraction,” *Science* **368**(6493), 885–889 (2020).
- ¹⁵ Y. Xiong, K.J. Wilkin, and M. Centurion, “High-resolution movies of molecular rotational dynamics captured with ultrafast electron diffraction,” *Phys. Rev. Research* **2**(4), 043064 (2020).
- ¹⁶ A. Kogar, A. Zong, P.E. Dolgirev, X. Shen, J. Straquadine, Y.-Q. Bie, X. Wang, T. Rohwer, I.-C. Tung, Y. Yang, R. Li, J. Yang, S. Weathersby, S. Park, M.E. Kozina, E.J. Sie, H. Wen, P. Jarillo-Herrero, I.R. Fisher, X. Wang, and N. Gedik, “Light-induced charge density wave in LaTe_3 ,” *Nat. Phys.* **16**(2), 159–163 (2020).
- ¹⁷ F. Qi, Z. Ma, L. Zhao, Y. Cheng, W. Jiang, C. Lu, T. Jiang, D. Qian, Z. Wang, W. Zhang, P. Zhu, X. Zou, W. Wan, D. Xiang, and J. Zhang, “Breaking 50 femtosecond resolution barrier in MeV ultrafast electron diffraction with a double bend achromat compressor,” *Phys. Rev. Lett.* **124**(13), 134803 (2020).
- ¹⁸ K. Amini, and J. Biegert, “Chapter Three - Ultrafast electron diffraction imaging of gas-phase molecules,” in *Advances In Atomic, Molecular, and Optical Physics*, edited by L.F. Dimauro, H. Perrin, and S.F. Yelin, (Academic Press, 2020), pp. 163–231.
- ¹⁹ M.R. Otto, J.-H. Pöhls, L.P.R. de Cotret, M.J. Stern, M. Sutton, and B.J. Siwick, “Mechanisms of electron-phonon coupling unraveled in momentum and time: The case of soft phonons in TiSe_2 ,” *Sci. Adv.* **7**(20), eabf2810 (2021).
- ²⁰ D. Filippetto, P. Musumeci, R.K. Li, B.J. Siwick, M.R. Otto, M. Centurion, and J.P.F. Nunes, “Ultrafast electron diffraction: Visualizing dynamic states of matter,” *Rev. Mod. Phys.* **94**(4), 045004 (2022).
- ²¹ M. Centurion, T.J.A. Wolf, and J. Yang, “Ultrafast imaging of molecules with electron diffraction,” *Annu. Rev. Phys. Chem.* **73**(1), 21–42 (2022).
- ²² W.H. Li, C.J.R. Duncan, M.B. Andorf, A.C. Bartnik, E. Bianco, L. Cultrera, A. Galdi, M. Gordon, M. Kaemingk, C.A. Pennington, L.F. Kourkoutis, I.V. Bazarov, and J.M. Maxson, “A kiloelectron-volt ultrafast electron micro-diffraction apparatus using low emittance semiconductor photocathodes,” *Struct. Dyn.* **9**(2), 024302 (2022).
- ²³ K. Amini, A. Rouzée, and M.J.J. Vrakking, *Structural Dynamics with X-Ray and Electron Scattering* (Royal Society of Chemistry, 2023).
- ²⁴ K.M. Siddiqui, D.B. Durham, F. Cropp, F. Ji, S. Paiagua, C. Ophus, N.C. Andresen, L. Jin, J. Wu, S. Wang, X. Zhang, W. You, M. Murnane, M. Centurion, X. Wang, D.S. Slaughter, R.A. Kaindl, P. Musumeci, A.M. Minor, and D. Filippetto, “Relativistic ultrafast electron diffraction at high repetition rates,” *Struct. Dyn.* **10**(6), 064302 (2023).
- ²⁵ T.M. Sutter, J.S.H. Lee, A.V. Kulkarni, P. Musumeci, and A. Kogar, “Vector-based feedback of continuous wave radiofrequency compression cavity for ultrafast electron diffraction,” *Struct. Dyn.* **11**(2), 024303 (2024).
- ²⁶ H. Mark, and R. Wierl, “Atomformfaktorbestimmung mit Elektronen,” *Zeitschrift Fur Physik* **60**, 741–753 (1930).
- ²⁷ H. Mark, and R. Wierl, “Über Elektronenbeugung am einzelnen Molekül,” *Naturwissenschaften* **18**(9), 205–205 (1930).
- ²⁸ I. Hargittai, and M. Hargittai, *Stereochemical Applications of Gas-Phase Electron Diffraction, Part A* (John Wiley & Sons, 1988).

- ²⁹ A.H. Zewail, "Laser femtochemistry," *Science* **242**(4886), 1645–1653 (1988).
- ³⁰ A.H. Zewail, "Femtochemistry: Atomic-scale dynamics of the chemical bond (Nobel Lecture)," *Angewandte Chemie International Edition* **39**(15), 2586–2631 (2000).
- ³¹ J.C. Williamson, M. Dantus, S.B. Kim, and A.H. Zewail, "Ultrafast diffraction and molecular structure," *Chem. Phys. Lett.* **196**(6), 529–534 (1992).
- ³² B.J. Siwick, J.R. Dwyer, R.E. Jordan, and R.J.D. Miller, "An atomic-level view of melting using femtosecond electron diffraction," *Science* **302**(5649), 1382–1385 (2003).
- ³³ L. Waldecker, R. Bertoni, and R. Ernstorfer, "Compact femtosecond electron diffractometer with 100 keV electron bunches approaching the single-electron pulse duration limit," *J. Appl. Phys.* **117**(4), 044903 (2015).
- ³⁴ L. Kasmi, D. Kreier, M. Bradler, E. Riedle, and P. Baum, "Femtosecond single-electron pulses generated by two-photon photoemission close to the work function," *New J. Phys.* **17**(3), 033008 (2015).
- ³⁵ G. Sciaini, M. Harb, S.G. Kruglik, T. Payer, C.T. Hebeisen, F.-J.M. zu Heringdorf, M. Yamaguchi, M.H. Hoegen, R. Ernstorfer, and R.J.D. Miller, "Electronic acceleration of atomic motions and disordering in bismuth," *Nature* **458**(7234), 56–59 (2009).
- ³⁶ B.J. Siwick, J.R. Dwyer, R.E. Jordan, and R.J.D. Miller, "Femtosecond electron diffraction studies of strongly driven structural phase transitions," *Chem. Phys.* **299**(2), 285–305 (2004).
- ³⁷ A. Zong, A. Kogar, Y.-Q. Bie, T. Rohwer, C. Lee, E. Baldini, E. Ergeçen, M.B. Yilmaz, B. Freelon, E.J. Sie, H. Zhou, J. Straquadine, P. Walmsley, P.E. Dolgirev, A.V. Rozhkov, I.R. Fisher, P. Jarillo-Herrero, B.V. Fine, and N. Gedik, "Evidence for topological defects in a photoinduced phase transition," *Nat. Phys.* **15**(1), 27–31 (2019).
- ³⁸ J. Yang, X. Zhu, T.J. Wolf, Z. Li, J.P.F. Nunes, R. Coffee, J.P. Cryan, M. Gühr, K. Hegazy, and T.F. Heinz, "Imaging CF₃I conical intersection and photodissociation dynamics with ultrafast electron diffraction," *Science* **361**(6397), 64–67 (2018).
- ³⁹ E.G. Champenois, N.H. List, M. Ware, M. Britton, P.H. Bucksbaum, X. Cheng, M. Centurion, J.P. Cryan, R. Forbes, I. Gabalski, K. Hegazy, M.C. Hoffmann, A.J. Howard, F. Ji, M.-F. Lin, J.P.F. Nunes, X. Shen, J. Yang, X. Wang, T.J. Martinez, and T.J.A. Wolf, "Femtosecond electronic and hydrogen structural dynamics in ammonia imaged with ultrafast electron diffraction," *Phys. Rev. Lett.* **131**(14), 143001 (2023).
- ⁴⁰ T. van Oudheusden, P.L.E.M. Pasmans, S.B. van der Geer, M.J. de Loos, M.J. van der Wiel, and O.J. Luiten, "Compression of subrelativistic space-charge-dominated electron bunches for single-shot femtosecond electron diffraction," *Phys. Rev. Lett.* **105**(26), 264801 (2010).
- ⁴¹ M.R. Otto, L.P. René de Cotret, M.J. Stern, and B.J. Siwick, "Solving the jitter problem in microwave compressed ultrafast electron diffraction instruments: Robust sub-50 fs cavity-laser phase stabilization," *Struct. Dyn.* **4**(5), 051101 (2017).
- ⁴² O. Zandi, K.J. Wilkin, Y. Xiong, and M. Centurion, "High current table-top setup for femtosecond gas electron diffraction," *Struct. Dyn.* **4**(4), 044022 (2017).
- ⁴³ M.R. Otto, L.P.R. de Cotret, D.A. Valverde-Chavez, K.L. Tiwari, N. Émond, M. Chaker, D.G. Cooke, and B.J. Siwick, "How optical excitation controls the structure and properties of vanadium dioxide," *Procl. Natl. Acad. Sci. U.S.A.* **116**(2), 450–455 (2019).
- ⁴⁴ C. Kealhofer, W. Schneider, D. Ehberger, A. Ryabov, F. Krausz, and P. Baum, "All-optical control and metrology of electron pulses," *Science* **352**(6284), 429–433 (2016).
- ⁴⁵ D. Ehberger, K.J. Mohler, T. Vasileiadis, R. Ernstorfer, L. Waldecker, and P. Baum, "Terahertz compression of electron pulses at a planar mirror membrane," *Phys. Rev. A* **11**(2), 024034 (2019).

- ⁴⁶ E.C. Snively, M.A.K. Othman, M. Kozina, B.K. Ofori-Okai, S.P. Weathersby, S. Park, X. Shen, X.J. Wang, M.C. Hoffmann, R.K. Li, and E.A. Nanni, “Femtosecond compression dynamics and timing jitter suppression in a THz-driven electron bunch compressor,” *Phys. Rev. Lett.* **124**(5), 054801 (2020).
- ⁴⁷ L. Ma, X. Shen, K. Kim, D. Brown, M. D’Ewart, B. Hong, J. Olsen, S. Smith, D. Van Winkle, E. Williams, S. Weathersby, X. Wang, A. Young, and J. Frisch, “SLAC UED LLRF system upgrade,” (2019).
- ⁴⁸ M. Volkov, E. Willinger, D.A. Kuznetsov, C.R. Müller, A. Fedorov, and P. Baum, “Photo-Switchable Nanoripples in $Ti_3C_2T_x$ MXene,” *ACS Nano* **15**(9), 14071–14079 (2021).
- ⁴⁹ S.R. Tauchert, M. Volkov, D. Ehberger, D. Kazenwadel, M. Evers, H. Lange, A. Donges, A. Book, W. Kreuzpaintner, U. Nowak, and P. Baum, “Polarized phonons carry angular momentum in ultrafast demagnetization,” *Nature* **602**(7895), 73–77 (2022).
- ⁵⁰ C. Kealhofer, S. Lahme, T. Urban, and P. Baum, “Signal-to-noise in femtosecond electron diffraction,” *Ultramicroscopy* **159**, 19–25 (2015).
- ⁵¹ I. González Vallejo, G. Gallé, B. Arnaud, S.A. Scott, M.G. Lagally, D. Boschetto, P.-E. Coulon, G. Rizza, F. Houdellier, D. Le Bolloc’h, and J. Faure, “Observation of large multiple scattering effects in ultrafast electron diffraction on monocrystalline silicon,” *Phys. Rev. B* **97**(5), 054302 (2018).
- ⁵² R.C. Blase, R.R. Benke, G.P. Miller, K.S. Pickens, and J.H. Waite, “Microchannel plate detector detection efficiency to monoenergetic electrons between 3 and 28 keV,” *Rev. Sci. Instrum.* **88**(5), 053302 (2017).
- ⁵³ P. Pasmans, D. Van Vugt, J. Van Lieshout, G. Brussaard, and O. Luiten, “Extreme regimes of femtosecond photoemission from a copper cathode in a dc electron gun,” *Phys. Rev. Accel. Beams* **19**(10), 103403 (2016).
- ⁵⁴ S. Fernandez-Perez, V. Boccone, C. Broennimann, C. Disch, L. Piazza, V. Radicci, M. Rissi, C. Schulze-Briese, P. Trueb, and P. Zambon, “Characterization of a hybrid pixel counting detector using a silicon sensor and the IBEX readout ASIC for electron detection,” *J. Inst.* **16**(10), P10034 (2021).
- ⁵⁵ P. Zambon, “Temporal and spatial variance in pixelated counting detectors with dead time and retrigger capability,” *Nuclear Instruments and Methods in Physics Research Section A: Accelerators, Spectrometers, Detectors and Associated Equipment* **1032**, 166625 (2022).
- ⁵⁶ F. Salvat, A. Jablonski, and C.J. Powell, “elsepa—Dirac partial-wave calculation of elastic scattering of electrons and positrons by atoms, positive ions and molecules (New Version Announcement),” *Comput. Phys. Commun.* **261**, 107704 (2021).
- ⁵⁷ CrystalMaker®, “Generated using CrystalDiffract®: a powder diffraction program for Mac and Windows. CrystalMaker Software Ltd, Oxford, England (www.crystallmaker.com),” (n.d.).
- ⁵⁸ D.F.J. Nijhof, T.C.H. de Raadt, J.V. Huijts, J.G.H. Franssen, P.H.A. Mutsaers, and O.J. Luiten, “RF acceleration of ultracold electron bunches,” *Struct. Dyn.* **10**(5), 054303 (2023).
- ⁵⁹ G. Sciaini, and R.D. Miller, “Femtosecond electron diffraction: heralding the era of atomically resolved dynamics,” *Rep. Prog. Phys.* **74**(9), 096101 (2011).
- ⁶⁰ C. Brönnimann, and P. Trüb, “Hybrid pixel photon counting X-ray detectors for synchrotron radiation,” in *Synchrotron Light Sources and Free-Electron Lasers: Accelerator Physics, Instrumentation and Science Applications*, edited by E. Jaeschke, S. Khan, J.R. Schneider, and J.B. Hastings, (Springer International Publishing, Cham, 2018), pp. 1–33.
- ⁶¹ P. Zambon, “Dead time model for X-ray photon counting detectors with retrigger capability,” *Nuclear Instruments and Methods in Physics Research Section A: Accelerators, Spectrometers, Detectors and Associated Equipment* **994**, 165087 (2021).

- ⁶² V. Morrison, Structural dynamics of the metal-insulator transition in VO₂: an ultrafast electron diffraction study with radio-frequency compressed electron pulses, PhD, McGill University, 2014.
- ⁶³ D. Kreier, Ultrafast single-electron diffraction at 100 keV and investigation of carbon-nanotube dynamics, PhD, Ludwig-Maximilians-Universität München, 2015.
- ⁶⁴ H. Park, X. Wang, S. Nie, R. Clinite, and J. Cao, “Direct and real-time probing of both coherent and thermal lattice motions,” *Solid State Commun.* **136**(9), 559–563 (2005).
- ⁶⁵ L. Wen-Xi, Z. Peng-Fei, W. Xuan, N. Shou-Hua, Z. Zhong-Chao, C. Rick, C. Jian-Ming, S. Zheng-Ming, and Z. Jie, “Ultrafast electron diffraction with spatiotemporal resolution of atomic motion,” *Chinese Phys. Lett.* **26**(2), 020701 (2009).
- ⁶⁶ R. Li, K. Sundqvist, J. Chen, H.E. Elsayed-Ali, J. Zhang, and P.M. Rentzepis, “Transient lattice deformations of crystals studied by means of ultrafast time-resolved x-ray and electron diffraction,” *Struct. Dyn.* **5**(4), 044501 (2018).
- ⁶⁷ J.K. Yu, C. Bannwarth, R. Liang, E.G. Hohenstein, and T.J. Martínez, “Nonadiabatic dynamics simulation of the wavelength-dependent photochemistry of azobenzene excited to the $\pi\pi^*$ and $\pi\pi^*$ excited states,” *J. Am. Chem. Soc.* **142**(49), 20680–20690 (2020).
- ⁶⁸ M.S. Schuurman, and A. Stolow, “Dynamics at conical intersections,” *Annu. Rev. Phys. Chem.* **69**(1), 427–450 (2018).
- ⁶⁹ S. Pathak, L.M. Ibele, R. Boll, C. Callegari, A. Demidovich, B. Erk, R. Feifel, R. Forbes, M. Di Fraia, L. Giannessi, C.S. Hansen, D.M.P. Holland, R.A. Ingle, R. Mason, O. Plekan, K.C. Prince, A. Rouzée, R.J. Squibb, J. Tross, M.N.R. Ashfold, B.F.E. Curchod, and D. Rolles, “Tracking the ultraviolet-induced photochemistry of thiophenone during and after ultrafast ring opening,” *Nat. Chem.* **12**(9), 795–800 (2020).
- ⁷⁰ L.P. René de Cotret, J.-H. Pöhls, M.J. Stern, M.R. Otto, M. Sutton, and B.J. Siwick, “Time- and momentum-resolved phonon population dynamics with ultrafast electron diffuse scattering,” *Phys. Rev. B* **100**(21), 214115 (2019).
- ⁷¹ J. Maxson, L. Cultrera, C. Gulliford, and I. Bazarov, “Measurement of the tradeoff between intrinsic emittance and quantum efficiency from a NaKSb photocathode near threshold,” *Appl. Phys. Lett.* **106**(23), 234102 (2015).
- ⁷² Y.-J. Kim, L.D. Palmer, W. Lee, N.J. Heller, and S.K. Cushing, “Using electron energy-loss spectroscopy to measure nanoscale electronic and vibrational dynamics in a TEM,” *J. Chem. Phys.* **159**(5), 050901 (2023).
- ⁷³ W. Verhoeven, J.F.M. van Rens, M. a. W. van Ninhuijs, W.F. Toonen, E.R. Kieft, P.H.A. Mutsaers, and O.J. Luiten, “Time-of-flight electron energy loss spectroscopy using TM₁₁₀ deflection cavities,” *Struct. Dyn.* **3**(5), 054303 (2016).
- ⁷⁴ W. Verhoeven, J.F.M. van Rens, W.F. Toonen, E.R. Kieft, P.H.A. Mutsaers, and O.J. Luiten, “Time-of-flight electron energy loss spectroscopy by longitudinal phase space manipulation with microwave cavities,” *Struct. Dyn.* **5**(5), 051101 (2018).
- ⁷⁵ D. Ehberger, C. Kealhofer, and P. Baum, “Electron energy analysis by phase-space shaping with THz field cycles,” *Struct. Dyn.* **5**(4), 044303 (2018).
- ⁷⁶ R.K. Li, and X.J. Wang, “Femtosecond MeV Electron Energy-Loss Spectroscopy,” *Phys. Rev. Appl.* **8**(5), 054017 (2017).
- ⁷⁷ X. Yang, W. Wan, L. Wu, V. Smaluk, T. Shaftan, and Y. Zhu, “Toward monochromated sub-nanometer UEM and femtosecond UED,” *Sci. Rep.* **10**(1), 16171 (2020).
- ⁷⁸ C.J. Duncan, D.A. Muller, and J.M. Maxson, “Lossless monochromation for electron microscopy with pulsed photoemission sources and radio-frequency cavities,” *Phys. Rev. Appl.* **14**(1), 014060 (2020).

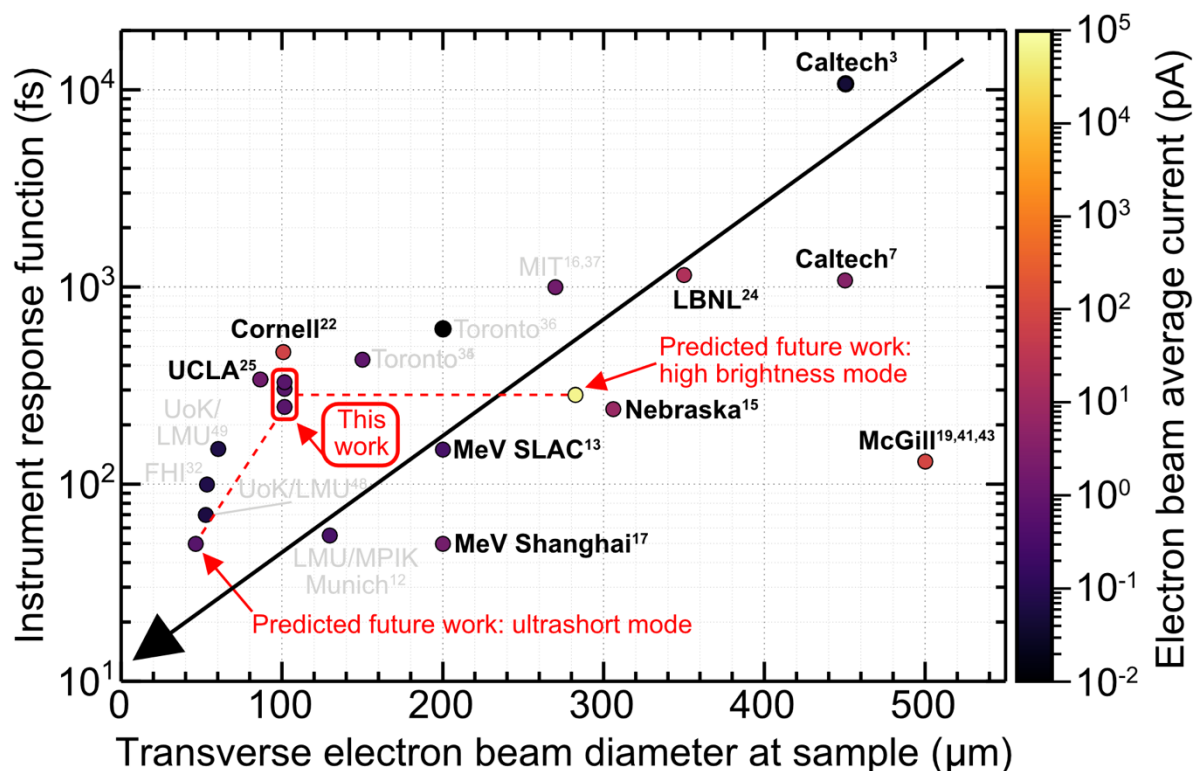


FIG. 1. Evolution of instrument response function and transverse electron beam diameter at the sample position as a function of the average current of the electron beam. All values are given as full width at half maximum (FWHM) values. The diagonal black arrow indicates the evolution of UED towards shorter and smaller electron pulses. The brightness of the electron beam is depicted by the z-scale colourmap representing the electron beam average current. Set-ups that are generally incompatible for gas-phase UED measurements are shown in grey text. Our work is highlighted by red text, arrows and rectangles. The anticipated future capabilities of our set-up are depicted by dashed lines, indicating the expected range of parameters.

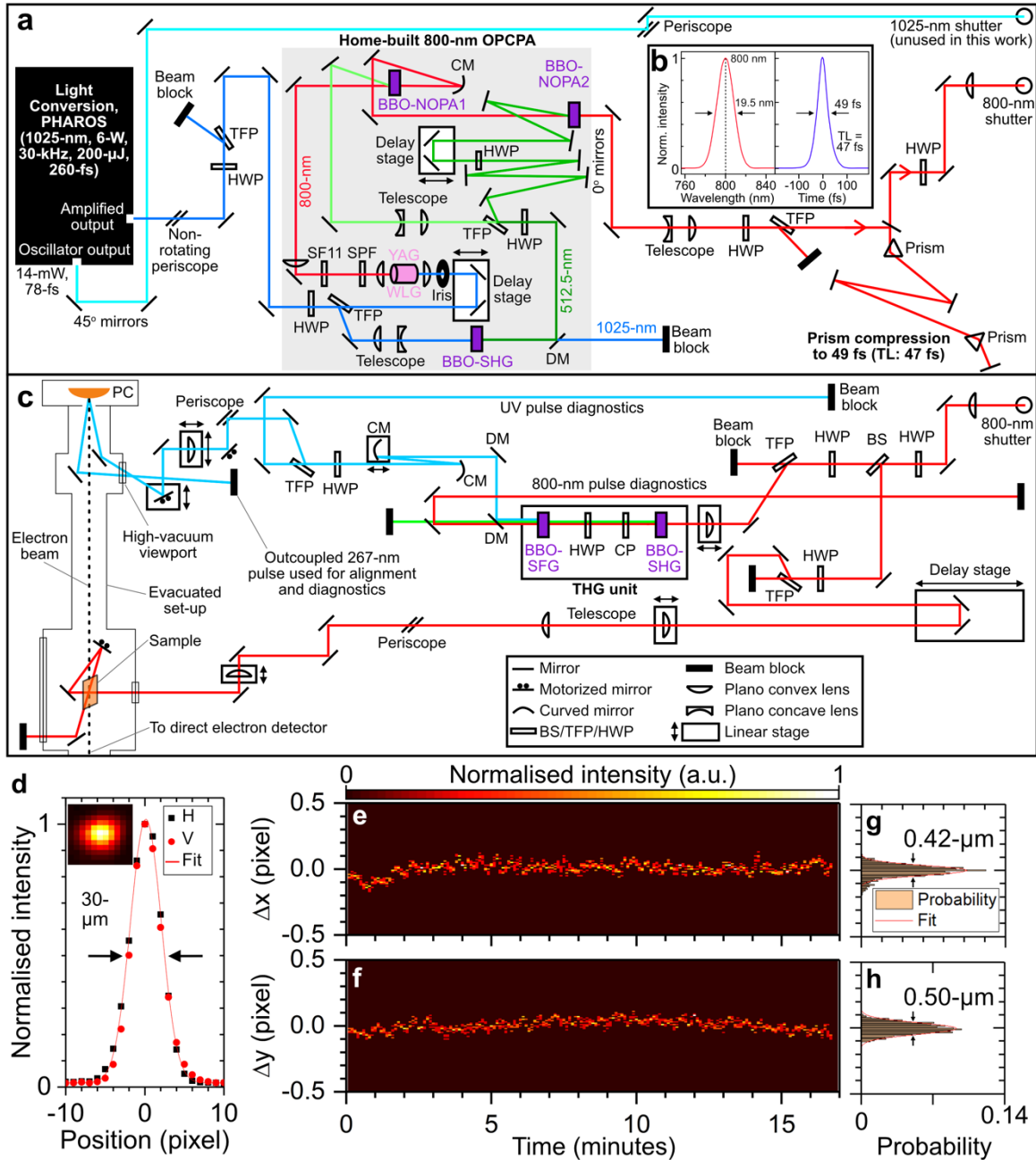


FIG. 2. (a) Schematic of a 30-kHz, home-built optical parametric chirped pulse amplification (OPCPA) system that employs a 6-W PHAROS laser system as the supercontinuum-seed and pump laser, and subsequent prism compression. (b) Wavelength and temporal profile of OPCA output reconstructed from frequency-resolved optical gating (FROG) measurements. The central wavelength, λ_c , and transform limit (TL) of the pulse are indicated. (c) Schematic of optical set-up for generating electron probe pulses using ultraviolet (UV) light at the photocathode (PC), and sample excitation using 800-nm optical pump pulses. (d) UV beam profile. Cuts along the horizontal (H) and vertical (V) axes are shown with a Gaussian fit. Inset: UV beam detector image. (e-f) UV beam pointing measurement. Changes in the (b) horizontal (Δx) and (c) vertical (Δy) position of the UV beam are shown. (g-h) Histogram distribution of the corresponding data shown in panel (b-c). Gaussian fits were applied to the histogram distributions.

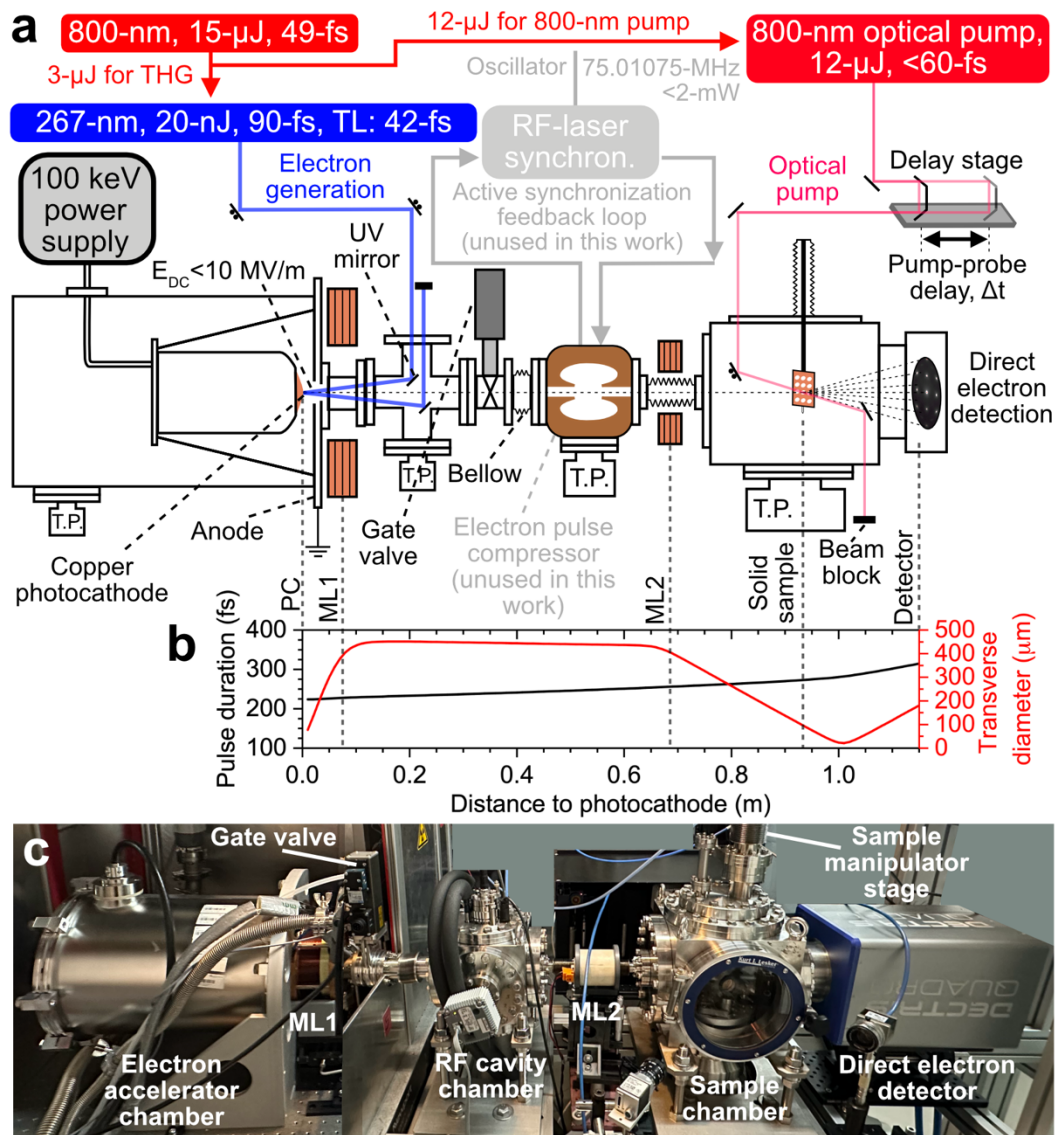


FIG. 3. (a) Schematic of the 30 kHz, 95 keV HiRep-UED instrument, with each component labelled. See main text for more details. (b) General Particle Tracer (GPT) simulation of the electron pulse duration (blue distribution) and transverse diameter (red distribution) with the instrument operating in the temporally uncompressed mode using an electron beam containing 55 electrons. All values are given in FWHM. (c) Image of the instrument in the laboratory.

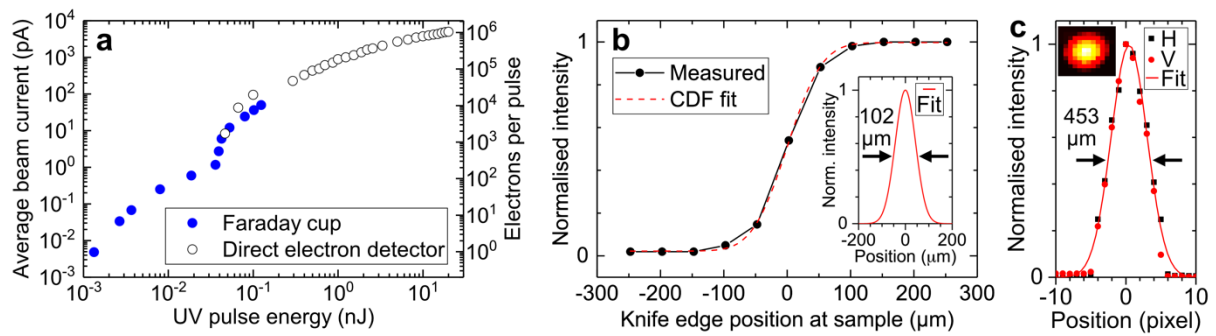


FIG. 4. (a) Average beam current and electrons per pulse as a function of UV pulse energy measured with a Faraday cup and direct electron detector, respectively. (b) Knife edge scan of electron beam at the sample position. A Gaussian cumulative distribution function (CDF) was fitted to the measured data. Inset: retrieved Gaussian distribution from CDF fit in panel (b). The FWHM electron beam diameter is indicated by black arrows. (c) Electron beam profile at the detector position obtained from the same data as in panel (b). Inset: electron detector image.

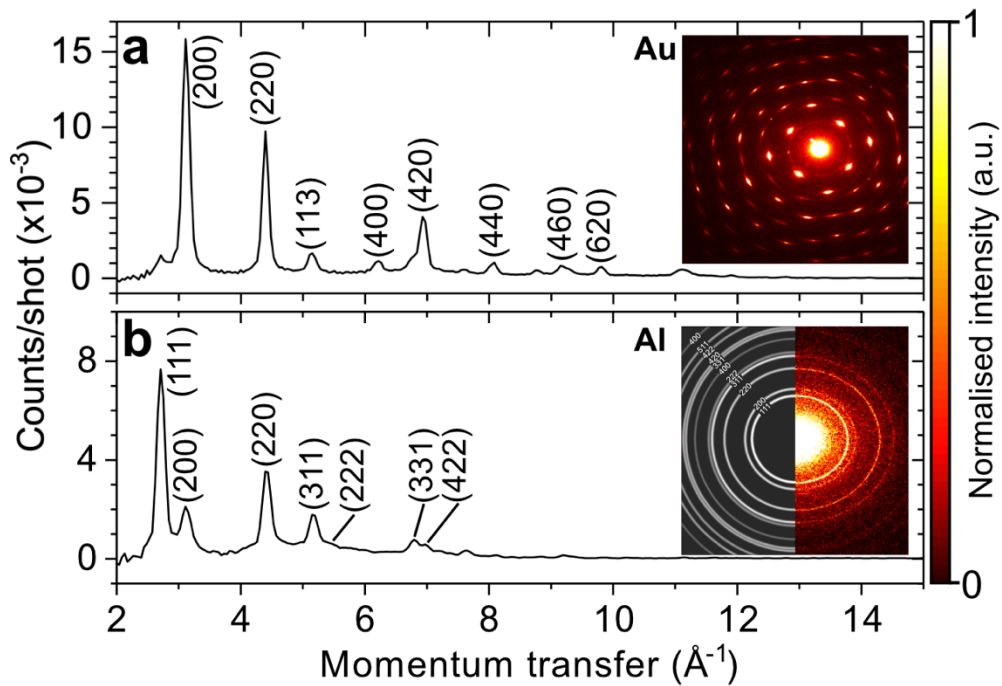


FIG. 5. (a-b) Electron diffraction patterns of (a) 11-nm monocrystalline gold (Au) and (b) 31-nm polycrystalline aluminium (Al) measured using a 95-keV electron pulse containing ~ 100 at 30-kHz with a direct electron detector. Both data were measured without apertures. Insets: measured detector images, with simulated data shown for aluminium.

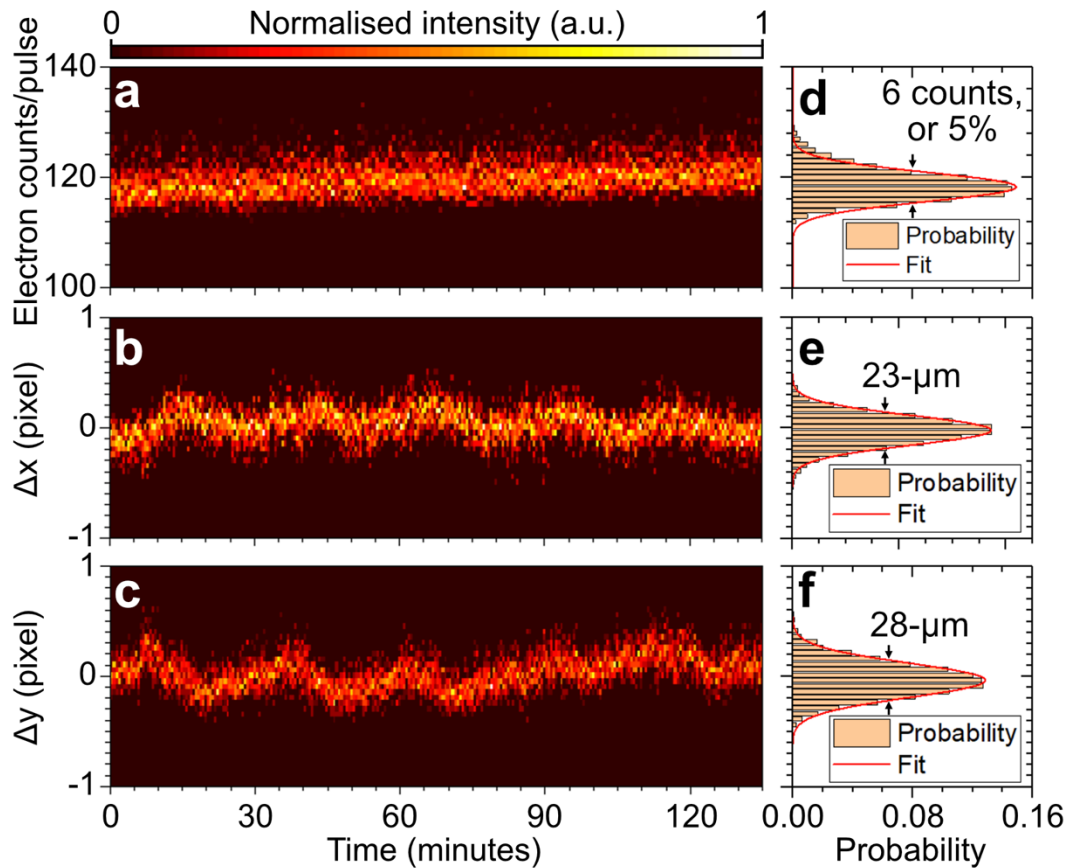


FIG. 6. (a-c) Two-dimensional plot of the (a) number of electron counts per pulse, and changes in the (b) x -centre position (Δx), and (c) y -centre position (Δy) as a function of time. A total of $\sim 8,100$ images were acquired, with each image capturing the electron beam, which had an average of ~ 110 electrons, over an exposure time of 1-s. (d-f) Histogram plots of the data corresponding to panels (a-c) with a Gaussian fit applied. All values are given in FWHM.

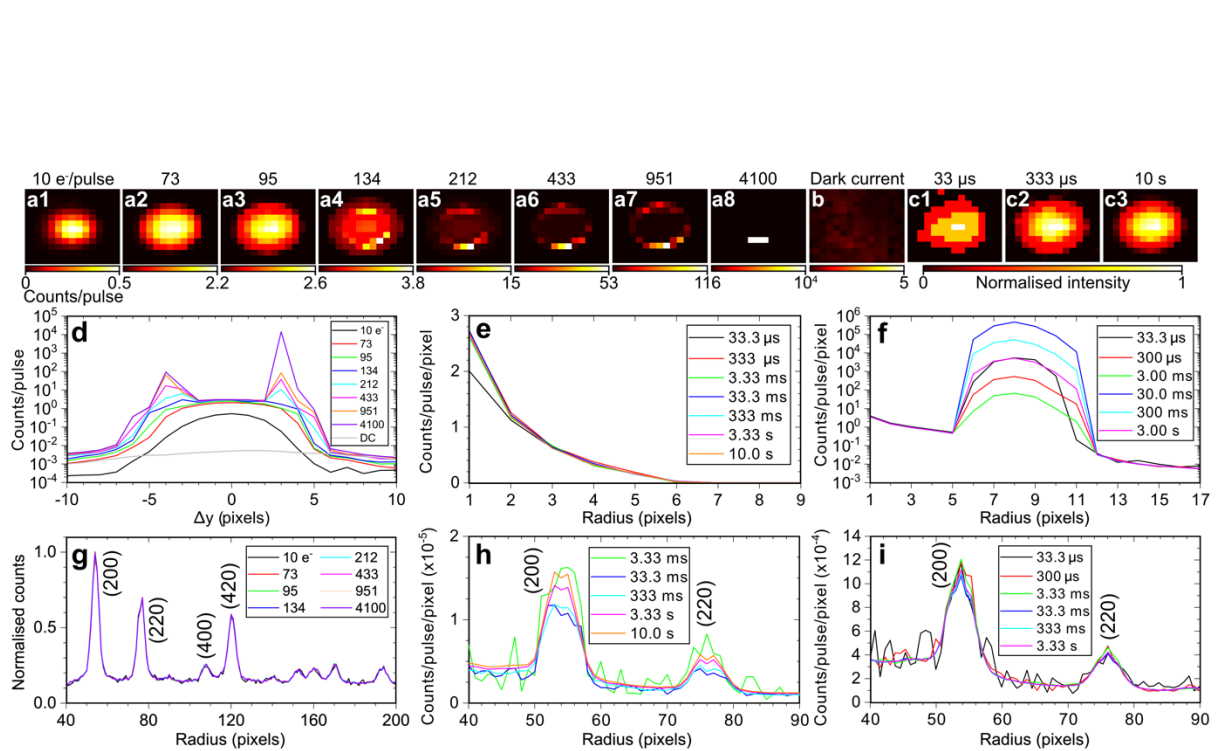


FIG. 7. Saturation effects in DECTRIS QUADRO direct electron detector. **(a1-a8)** Detector images measured with a different number of electrons per pulse as indicated at the top of images 1-8. Exposure time of 0.1-s was used. **(b)** Detector image of dark current contribution with a colourmap scaling that was multiplied by a factor of 10 relative to that of image a1. Exposure time of 0.1-s was used. **(c1-c3)** Detector images of an electron beam containing 10^2 electrons measured with different exposure times. **(d)** Vertical beam profile of the primary unscattered electron beam after interaction with an 11-nm monocrystalline gold sample using an electron pulse containing different numbers of electrons. **(e-f)** Radial distribution of electron beam measured with different exposure times using an electron beam containing (d) 10^2 electrons and (e) 10^4 electrons. **(g-i)** Radial distributions of Bragg diffraction peaks from the sample corresponding to data from panels (d-f). Panel (g) was normalised to the sum of the total intensity corresponding to a radius of 30 – 200 pixels for a like-for-like comparison of data measured with different number of electrons. Panels (a,b,d,g) were averaged over 100 images, while all other panels were measured with a single image.

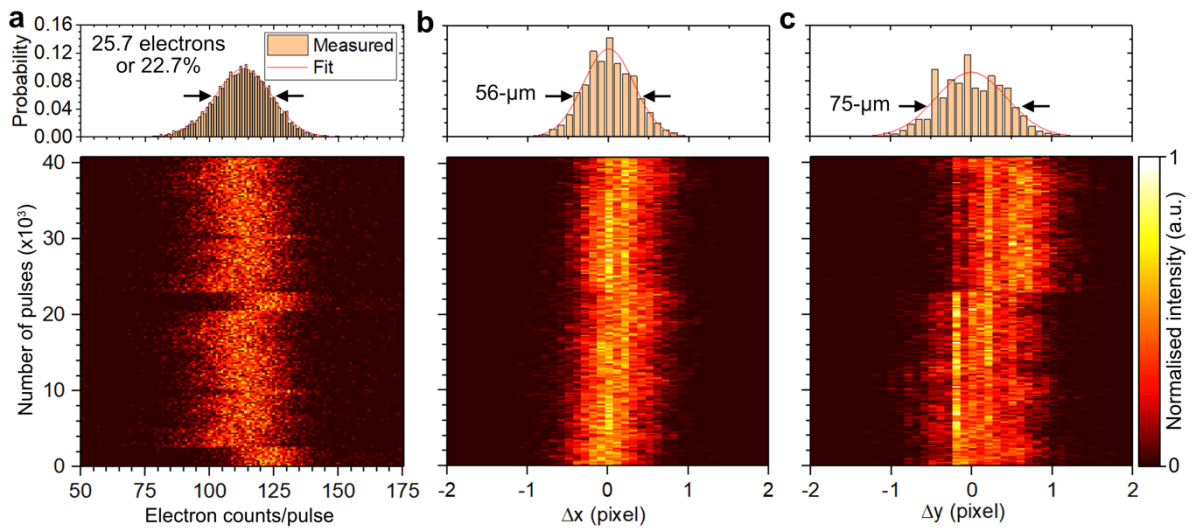


FIG. 8. Shot-to-shot analysis. **(a)** Two-dimensional plot of the number of electrons per shot as a function of number of pulses. An electron beam containing an average of 113 electrons was measured with an exposure time of 33.3- μs . A total of 40,000 images were recorded. A histogram plot of the associated data is shown at the top of the panel with a Gaussian fit applied. **(b-c)** Same as in panel (a) but for changes in the x (b) and y (c) centre positions of the electron beam.

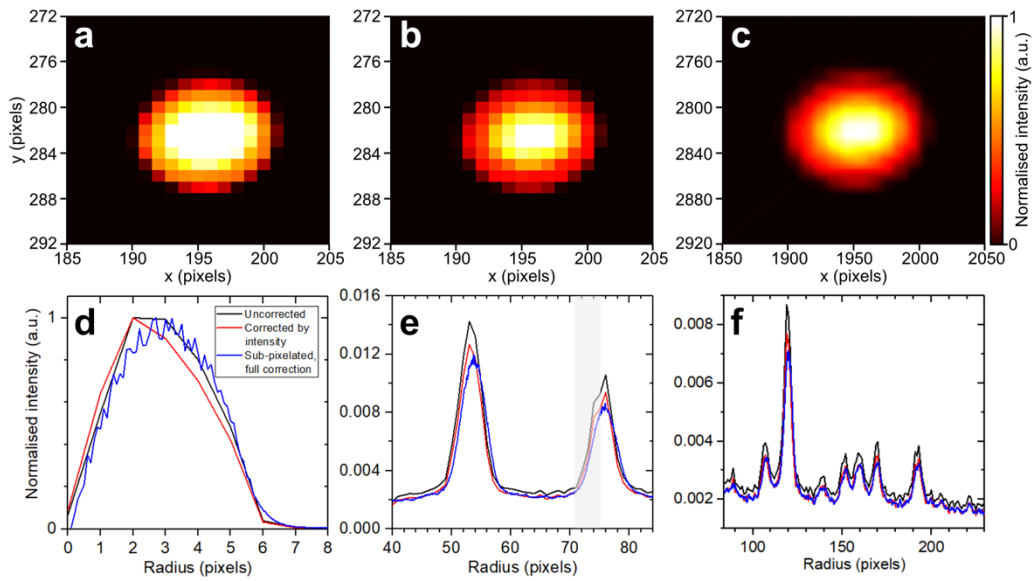


FIG. 9. Shot-to-shot correction of electron beam pointing and intensity jitter with sub-pixel accuracy. **(a-c)** Summed detector image of electron beam (a) before any correction, (b) after intensity jitter correction, and (c) after intensity and pointing jitter correction with sub-pixelation of factor 10. The images shown were summed over $\sim 40,000$ shots corresponding to the data shown in Figure 8. **(d)** Radial distribution of primary unscattered electron beam before and after correction. **(e-f)** Radial distribution of Bragg diffraction peaks from 11-nm monocrystalline gold before and after correction.

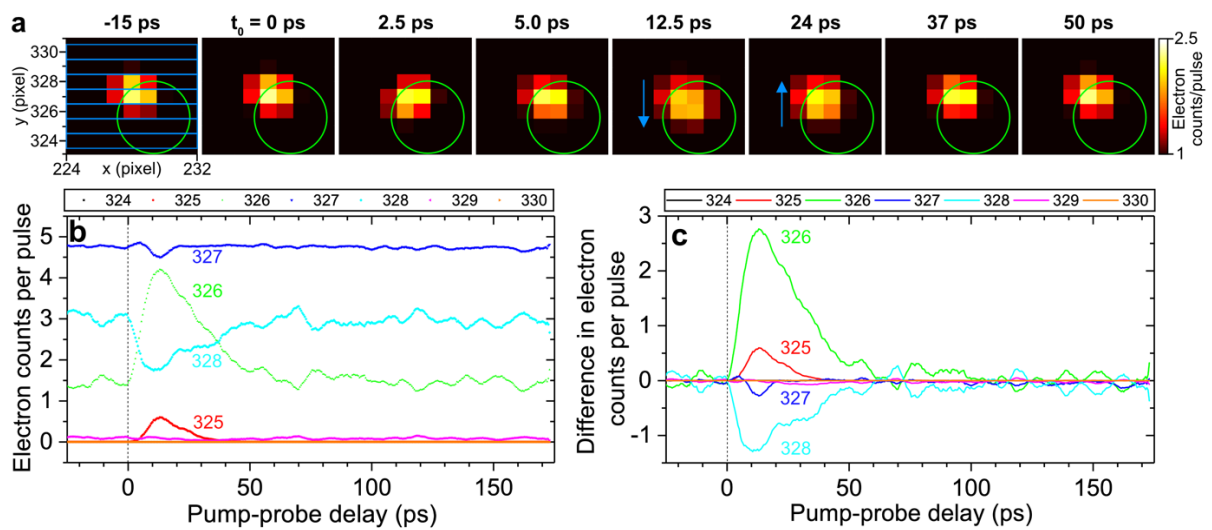


FIG. 10. Finding time-zero overlap between the optical-pump and electron-probe pulses by space-charge deflection of the electron beam. **(a)** Detector images of an electron pulse containing 55 electrons measured at different pump-probe delay times passing through a copper meshgrid (300 lines/inch) with a 100- μm copper aperture placed in-front of the meshgrid. Green circles highlight the observed time-resolved changes in the electron beam profile caused by photoelectrons generated by an optical pump pulse focussed to a $\sim 100\text{-}\mu\text{m}$ diameter spot on the meshgrid with a fluence of 52 mJ/cm^2 . **(b)** Electron counts per shot integrated across different horizontal strips of the detector image corresponding to a specific y -pixel integrated over a fixed x -pixel range of 224-232 (see blue shaded rectangles in panel (a) at -15 ps). **(c)** Same as in panel (b) but with the average counts at negative delays subtracted in each y -pixel horizontal strip.

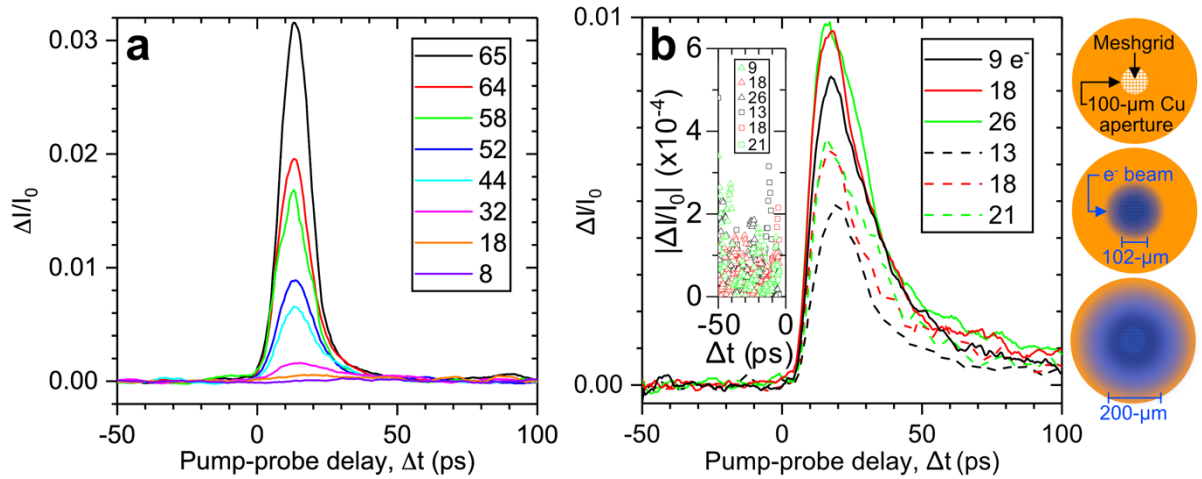


FIG. 11. (a) Difference in pump-probe signal relative to the reference probe-only signal, $\Delta I/I_0$, as a function of pump-probe delay at different pump fluences. The $\Delta I/I_0$ signal was integrated across a circular region of interest with radius of four pixels, and was corrected for fluctuations in electron beam intensity. At all fluences, an electron beam containing 55 electrons had nine electrons passing through a 100- μm aperture placed in front of the meshgrid sample. The values of fluences are given in mJ/cm^2 . **(b)** The $\Delta I/I_0$ signal as a function of pump-probe delay for an electron beam containing a varied number of electrons but with two different FWHM transverse diameters of 102- μm (solid distributions) and 200- μm (dashed) at the sample position. The number of electrons in the beam that passed through the 100- μm aperture are given in the legend. The inset shows the absolute values of the difference contrast signal, $|\Delta I/I_0|$, at negative pump-probe delays. A schematic of the aperture, meshgrid and electron beam size is shown on the right-hand side. The $\Delta I/I_0$ signal was measured at a constant pump fluence of 52 mJ/cm^2 .

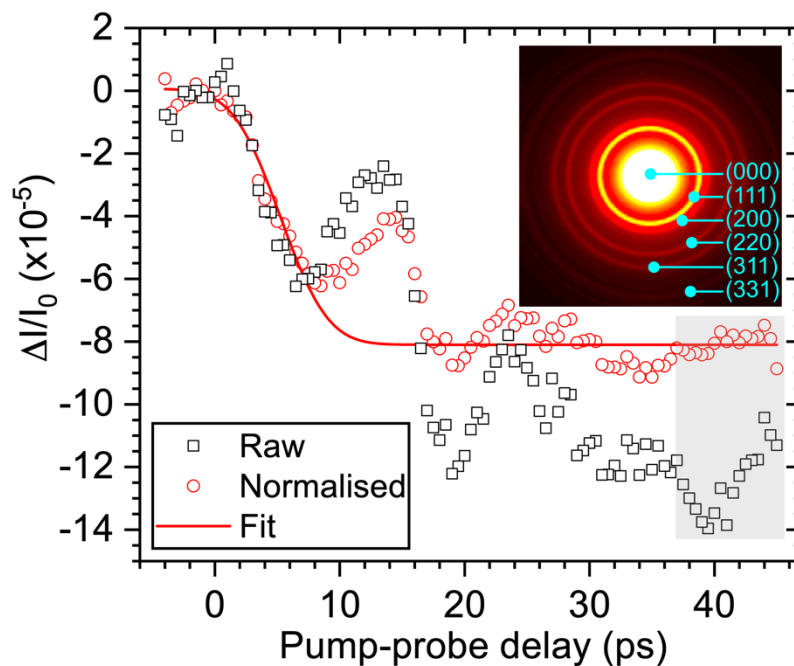


FIG. 12. The $\Delta I/I_0$ signal of (331) diffraction peak in 31-nm polycrystalline aluminium optically excited by an 800-nm pump pulse with a fluence of 1 mJ/cm². Measured data is shown before (black squares) and after (red circles) normalising the electron intensity by the unscattered primary electron beam intensity at each pump-probe step. The grey shaded area shows the importance of correcting for fluctuations in the electron beam intensity. A fit to the step-function decrease in the normalised $\Delta I/I_0$ signal is shown as the red distribution. The inset shows the diffraction image of aluminium, with the (000) unscattered signal labelled together with the first five diffraction rings. The impact of correcting for intensity fluctuations in the electron beam is highlighted by the grey shaded area.

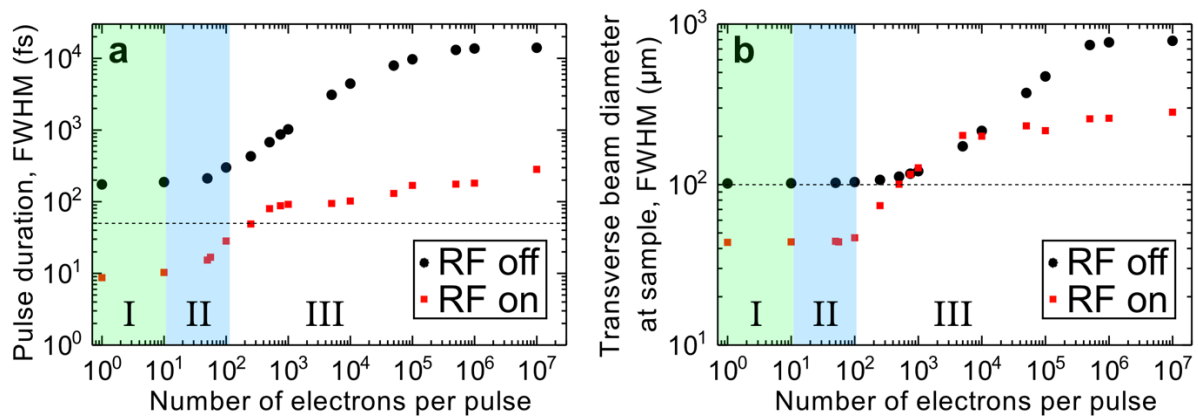


FIG. 13. (a-b) General particle tracer (GPT) simulations of the (a) pulse duration and (b) transverse beam diameter of an electron pulse containing a varied number of electrons at the sample. All values are given in FWHM. Simulated data are shown with the radiofrequency (RF) cavity on (black circles) and off (red squares) where the electron beam is temporally compressed and uncompressed, respectively. The UV pulse duration used in the simulations was 90-fs (60-fs) FWHM with the RF cavity on (off). Three regions of space-charge are indicated: (I) no-to-low space-charge (green shaded), (II) low-to-moderate space-charge (blue shaded), and (III) severe space-charge dispersion. Horizontal dashed lines indicate thresholds for an electron beam with a 50-fs duration and a 100- μ m transverse diameter at the sample.

Supplementary Information

S1. EXPERIMENTAL

A. UV-photocathode alignment procedure

As a first alignment step, the UV lens was removed and the aperture of an iris positioned before the first piezo-mounted mirror was reduced to a <1-mm diameter size. Using the maximum UV pulse energy available (20-nJ), the unfocussed UV beam impinged on the 1-mm flat part of the photocathode only when the outcoupled UV beam reflected by the second, rectangular in-vacuum UV mirror shows the machining grooves of the photocathode (see Fig. S1a). Moreover, an electron pulse could be measured with the electron detector without the UV lens inserted. To correctly align the UV pulse onto the flat part of the photocathode, the input and outcoupled UV beam crossed each other using the two fixed in-vacuum UV mirrors of the electron accelerator set-up (formerly AccTec BV, now known as Doctor X Works BV).

As a second alignment step, the UV lens was re-inserted and aligned along the optical axis such that there was no coma or astigmatism present in the UV beam profile at the focus. The last piezo-mounted mirror and the UV lens were both mounted to their own respective linear stage, enabling fine adjustment to achieve optimal spatial alignment perpendicular to the optical axis. At the optimal alignment, the brightest outcoupled UV beam was reflected by the second, rectangular in-vacuum UV mirror, which also exhibited machining grooves of the photocathode (see Fig. S1b). A systematic examination of the unfocussed electron beam profile was conducted with the detector positioned as close as feasible to the photocathode (photocathode-detector distance of ~0.5-m). An optimal electron beam profile was determined by translating the last piezo-mounted UV mirror across a $2 \times 2 \text{ mm}^2$ area of the photocathode central flat region. The second last piezo-mounted UV mirror was then adjusted by a relatively large step, and the two-dimensional scan across a $2 \times 2 \text{ mm}^2$ area of the photocathode repeated with the last piezo-mounted mirror. This overall alignment procedure was repeated until the smallest electron beam diameter was obtained which remained consistently small across different positions of the 30- μm UV beam on the 1-mm flat portion of the photocathode. Furthermore, optimization of the UV lens position along the optical axis and adjustment of the distance between the two curved UV mirrors were performed to obtain a symmetrical and minimized electron beam profile.

Precise spatial alignment of the 800-nm optical pump and electron probe pulses was ensured by utilizing a 100- μm diameter copper aperture placed in-front of a meshgrid sample. Optimal alignment is achieved by optimizing the number of detected electrons (nine electrons passing through the aperture) and obtaining a symmetrical image of the meshgrid on a near-infrared sensitive card when the optical pulse passes through the aperture (see image in Fig. S1c measured with a camera). This alignment process utilizes an in-vacuum piezo-driven mirror to fine-tune the optical pulse alignment through the aperture.

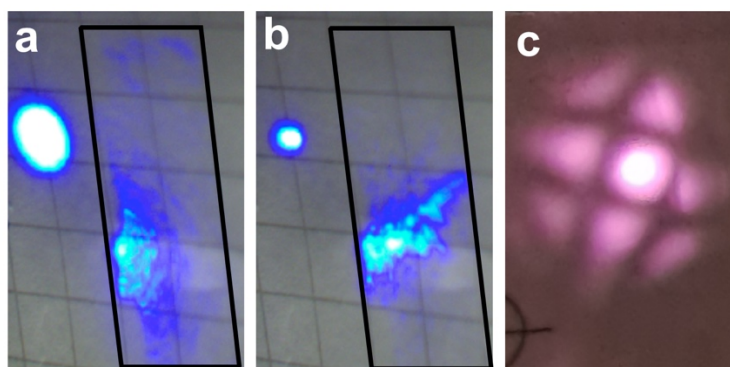


FIG. S1 (a-b) Photos of UV-induced fluorescence on a piece of paper (a) with and (b) without a UV lens positioned before the input CF40 UVFS window measured with a camera. The outcoupled UV beam using the in-vacuum rectangular mirror (see tilted black rectangle) is shown with the back-reflection of the UV beam reflected by the input CF40 UVFS window (see circular beam profile). **(c)** Outcoupled 800-nm pump pulse that passed through a meshgrid sample (300 lines/inch) with a 100- μm diameter copper aperture placed in-front of the meshgrid for alignment purposes.

B. HiRep-UED instrument

The footprint of the HiRep-UED instrument is approximately 1.5-m \times 1.0-m. The electron accelerator chamber with the six-way laser in-coupler unit (Doctor X Works BV, formerly AccTec BV; see Fig. 2c) is mounted onto an optical table (3-m \times 2-m), and is completely surrounded by X-ray radiation shielding comprised of ≥ 4 -mm thick lead shielding (attenuating the X-ray dosage by four-to-five orders of magnitude reduces the radiation levels outside the shielding to $\ll 1$ - $\mu\text{Sv/hr}$). The rest of the instrument is supported by a frame (~ 1.0 -m \times 0.5-m). This frame is equipped with rubber feet to minimize vibrations from the surrounding area. Each evacuated chamber is mounted on sliding plates attached to two longitudinal profiles that are secured to the frame. This design enables the chambers to be positioned anywhere along the frame, providing flexibility in placement, such as adjusting the distance between the detector and the photocathode. Bellows are incorporated between chambers to provide flexibility in adjusting their positions relative to each other. Each high-vacuum chamber was evacuated by turbomolecular pumps with a base background pressure of $< 7 \times 10^{-7}$ mbar in the electron accelerator chamber (Edwards EXT 75DX) and the laser in-coupling six-way cross (Edwards EXT 75DX), and $< 3 \times 10^{-8}$ mbar in the radiofrequency (RF) cavity (Edwards nEXT 85D) and sample (Edwards nEXT 300) chambers. An existing 1,600 l/s turbomolecular pump (Edwards STPIXR1606) planned for future gas-phase measurements was capable of achieving $< 9 \times 10^{-10}$ mbar base pressure in the sample chamber. All turbomolecular pumps are pre-pumped by a 500 l/s dry vacuum pump (Edwards EPX 500LE) that can reach a base pressure of $< 10^{-4}$ mbar. A high vacuum gate valve (MAC N-7557-019) is employed after the electron accelerator to prevent the vacuum from being compromised (and to avoid high voltage breakdown issues) in the accelerator when, for example, operating the quick access door (Kurt J. Lesker) in the sample chamber to change samples. Two out-of-vacuum charge-coupled device (CCD) cameras are used to view the sample holder and to monitor the out-coupled optical pump pulse, both crucial to achieving optimal pump-probe spatial overlap.

Breakdown and arcing issues with this electron accelerator were circumvented through the following steps. The aluminium housing that supports the copper cathode was polished to mirror finish using diamond paste (from 3- μm to 0.25- μm). The high-vacuum chamber supporting the cathode assembly was also electropolished. Replacement of the copper photocathode (Doctor X Works BV) is recommended for every six-to-twelve months of operation, which has a significant impact on the electron beam's emittance properties.⁶⁵ After replacing the photocathode or breaking high-vacuum conditions in the accelerator, the photocathode was trained, over a 48-hour period, to hold a voltage of 100-keV (the maximum voltage of the power supply), where many breakdown events occurred to reach 100-keV. Crucially, the conditioning of the electron accelerator was performed with a relatively high current (*i.e.*, 100- μA) and a low voltage rate (*i.e.*, <0.5-kV/minute). Daily stable operation of the electron accelerator at 95-keV was possible by slowly increasing the voltage to 95-keV in steps of 1-kV/minute over ~1.5 hours, held at a current of 10- μA .